JOURNAL OF SPACECRAFT AND ROCKETS
Vol. 47, No. 5, September–October 2010

Ablation and Thermal Response Property Model Validation for Phenolic Impregnated Carbon Ablator

F. S. Milos* and Y.-K. Chen†
NASA Ames Research Center, Moffett Field, California 94035-1000

DOI: 10.2514/1.42949

Phenolic impregnated carbon ablator was the heat-shield material for the Stardust probe and was considered as a candidate heat-shield material for the Orion Crew Module. As part of the heat-shield qualification for Orion, physical and thermal properties were measured for newly manufactured material, including emissivity, heat capacity, thermal conductivity, elemental composition, and thermal decomposition rates. Based on these properties, an ablation and thermal-response model was developed for temperatures up to 3500 K and pressures up to 100 kPa. The model includes transversely isotropic and pressure-dependent thermal conductivity. In this work, model validation is accomplished by comparison of predictions with data from many arcjet tests conducted over a range of stagnation heat flux and pressure from 107 W/cm^2 at 2.3 kPa to 1100 W/cm^2 at 84 kPa. Over the entire range of test conditions, model predictions compare well with measured recession, maximum surface temperatures, in-depth temperatures, and char depth.

Nomenclature

A, B, C, D	=	four thermocouple placement options
E	=	fractional error in recession
X, Y	=	Cartesian coordinates perpendicular to Z, cm
Z	=	Cartesian coordinate parallel to the axis of the geometry, cm
ΔS	=	centerline recession, mm
I, II, III	=	three model geometry options

I. Introduction

PHENOLIC impregnated carbon ablator (PICA) [1] is one of the lightweight ceramic ablators invented at NASA Ames Research Center (ARC) in the 1990s. PICA was the heat-shield material on the Stardust sample-return capsule [2], which is the fastest man-made Earth-entry vehicle to date. PICA is the forebody heat-shield material for the Mars Science Laboratory [3], and it was one of two candidate materials for the Orion Crew Module [4]. A similar material, named PICA-X, is manufactured by SpaceX for use as the heat shield of the Dragon spacecraft.‡

The first thermal-response and ablation model for PICA was created for preflight analyses of Stardust [5]. Several years later, the model was updated [6,7]. More recently, the Orion thermal protection system (TPS) Advanced Development Project (ADP) conducted extensive thermal, mechanical, and general property testing of newly manufactured PICA. Based on data from these recent tests on new material, the PICAv3.3 material property model was developed.§ The PICAv3.3 model was created specifically for use with the Fully Implicit Ablation and Thermal-Response (FIAT) code [8] and the Two-Dimensional Implicit Thermal-Response and Ablation (TITAN) code [9,10]. These codes have been used with the PICAv3.3 model for analysis of ground tests as well as for thermal analysis and sizing of PICA for flight applications on Orion [10], Mars Science Laboratory [11], and Dragon.

A large number of arcjet tests were performed to acquire data on PICA thermal and ablative performance over a wide range of aerothermal conditions applicable to Orion low-Earth-orbit and lunar-return entries. Concurrent with the aforementioned testing, the PICAv3.3 model was validated by comparison of numerical predictions with this large database of arcjet test data. The purpose of this work is to document a representative portion of these validation studies, and in particular to demonstrate to what extent the analyses agree or disagree with the data from the arcjet tests.

II. Material Properties

PICA is a composite material made from a low density, rigid, carbon fiber insulation (Fiberform® from Fiber Material, Inc.) impregnated with a commercial phenolic resin. The density of both components may vary depending on the material processing employed. For application to the Orion heat shield, large quantities of PICA were needed. Therefore, the manufacturing capability was scaled up and tailored to produce consistent material in a specific density range. The Orion TPS ADP conducted extensive property testing of newly manufactured PICA. For virgin PICA, in general, multiple samples of material from different manufacturing lots were tested. Some properties were measured for arcjet and furnace-generated chars and also for the Fiberform substrate. This testing provided a database of material properties for PICA model development.

Virgin and char density and elemental composition were measured at room temperature. The emissivity was derived from spectral reflectance measurements of virgin material and of arcjet chars. Heat capacity and thermal conductivity were measured over a range of temperatures up to approximately 500 K. The heat capacity of virgin and char were consistent with known values for graphitic carbon and phenolic polymer. The thermal conductivity was found to be transversely isotropic (orthotropic with a plane of isotropy) and also weakly pressure-dependent because the material is porous. Thermal decomposition was measured at three heating rates and then curve fit using a three-reaction model. Pyrolysis gas enthalpy was calculated using the Multicomponent Ablation Thermochemistry (MAT) code [12] and assuming a transition from frozen composition at low

Presented as Paper 2008-262 at the 47th AIAA Aerospace Sciences Meeting, Orlando, FL, 5–8 January 2009; received 26 December 2008; revision received 29 July 2010; accepted for publication 13 August 2010.

*Aerospace Engineer, Thermal Protection Materials Branch, Mail Stop 234-1. Senior Member AIAA.

†Aerospace Engineer, Aerothermodynamics Branch, Mail Stop 230-2. Member AIAA.

‡SpaceX press release available at http://www.spacex.com/press.php?page=20090223 [retrieved 21 Aug. 2010].

§Milos, F. S., and Chen, Y.-K., "Ablation and Thermal Property Model for Phenolic Impregnated Carbon Ablator (PICA)," NASA TM-2009-215377, January 2009.

temperature to equilibrium composition at high temperature. Equilibrium thermochemical ablation tables were calculated using MAT for varying atmospheres (nitrogen-oxygen and air-argon mixtures) applicable to arcjet and flight environments. Some high temperature thermal properties were estimated. Specifically, the char heat capacity was assumed to be that of graphitic carbon. Also, the high temperature thermal conductivity was first estimated and then adjusted at three temperatures by comparison of one-dimensional FIAT model predictions with arcjet near-surface thermocouple data in a manner similar to that described in [6].

For a carbonaceous material such as PICA, equilibrium ablation is a good assumption for surface temperatures of 2000 K or greater, corresponding to heat fluxes above approximately 90 W/cm^2, and if the pressure is not so low that gas-phase kinetics limit the concentration of atomic oxygen near the surface. For surface temperatures below 2000 K, an equilibrium ablation model typically will overestimate the recession rate of carbon, because the surface oxidation rate becomes kinetically limited. Nonequilibrium ablation of PICA is discussed in more detail in [13].

III. Arcjet Models and Test Conditions

Figure 1 shows the calorimeter and model shape used in recent arcjet testing. This nose radius equals the diameter, the shoulder radius is 1/16 of the diameter, and the sides are cylindrical. The primary advantage of this "iso-q" geometry, compared with the more traditional flat-faced geometry, is that in the ARC arcjets the heat flux distribution is relatively constant over most of the front face. A typical computational fluid dynamics (CFD) calculation for a 10.16-cm-diam iso-q shape is provided in Fig. 2. This solution was calculated using the Data-Parallel Line Relaxation (DPLR) Navier–Stokes code [14] that has been used extensively for simulation of arcjet flowfields [15]. The calculated heat flux varies only 10% on the front face. The heat flux on the cylindrical side, as shown by the dashed curve, is 10 to 20% of the stagnation-point value for 5 cm beyond the shoulder. This magnitude of heating is not negligible;

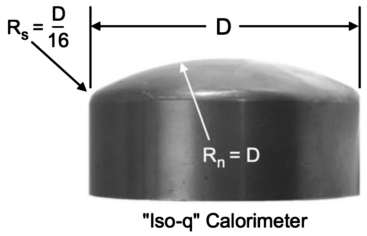

Fig. 1 Model shape for stagnation arcjet tests. TPS samples have the same external shape as the calorimeter used to measure the heat flux and stagnation pressure.

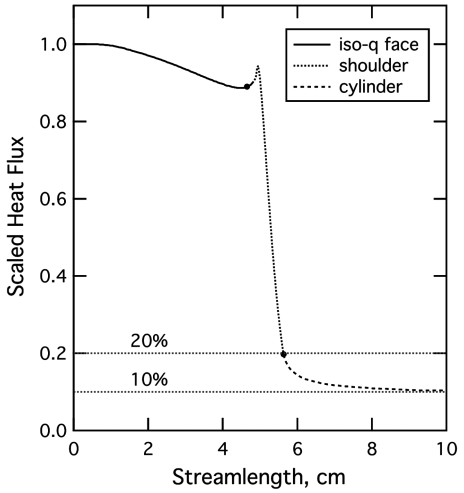

Fig. 2 Normalized heat flux distribution for sample with iso-q shape.

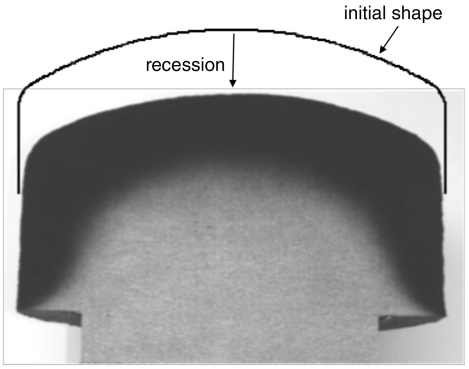

Fig. 3 Cross section of iso-q model AT-008 tested for 200 s. The ablated shape, after 13 mm of recession, is comparable to the initial shape.

therefore, it is to be expected that a nonnegligible heat load passes in through the cylindrical sides of the model.

Figure 3 presents a cross section of a PICA sample that was tested for 200 s and that experienced 13 mm of recession at the centerline. The black curve shows the initial unablated shape. The sidewall heating had sufficient magnitude to produce a substantial char depth and some recession, as evidenced by the slightly canted sides. Nevertheless, the ablated shape is comparable to the initial shape.

Figure 4 contains cross-sectional drawings of types I, II, and III of iso-q arcjet models used in this study. All models had a 10.16 cm diameter, except for one condition at 970 W/cm^2, where the diameter was 7.62 cm. In general, the exposed surface was machined PICA, and all unexposed PICA surfaces were sealed or bonded to adjacent materials using RTV-560 adhesive. Small spaces may be air gaps or partially filled with various adhesives. The LI2200 is an insulative silica-fiber tile material. Type I models are uninstrumented and were used in some initial screening tests. Most tests used type II models. For heat fluxes above 700 W/cm^2 the type III models with a silica-phenolic collar were used, because the sidewall heating is too high for the LI-2200 tile, which would melt excessively.

Most models of types II and III contained a press-fit plug with five thermocouples (TCs), as illustrated in Fig. 5. The plug diameter was 2.54 cm. The two thermocouples closest to the surface were type R, and the three deeper thermocouples were type K. Thermocouple wire with 0.25 mm diameter was inserted into 0.30 mm holes drilled perpendicular to the axis. The thermocouple junctions were centered at the axis. Grooves on the sides of the plug accommodated ceramic sleeves for the thermocouple wires. This installation method, with bare sensor wires approximately parallel to the heated surface, and with wire length-to-diameter ratio of at least 25:1 on each side of the TC junction, minimizes the measurement error due to temperature gradients along the length of the wires [16].

A few models also had offaxis thermocouples at two depths at locations depicted in Fig. 6. The offaxis thermocouples were installed using curved plugs that enabled sufficient lengths of thermocouple wire to be placed in concentric arcs at various radii from the axis in a manner consistent with the same ASTM International standard [16]. These thermocouples were unsheathed type K with 0.25 mm diameter. Because of spatial constraints for installation, thermocouples could not be placed at all ten locations within a single model. Some models contained thermocouples at locations 1 to 5, whereas others contained thermocouples at locations 6 to 10. Figure 7 presents X-ray images of an arcjet model with offaxis thermocouples. The thermocouple junctions are indicated by red dots. The thermocouples are not coplanar, and location 10 had three thermocouples located at different circumferential angles.

Overall, there were four different nominal placements for the thermocouples, as denoted by letters A to D in Table 1. For placements A to C the nominal spacing for axial thermocouples TC1 to TC4 was 0.381 cm. Placement A with TC1 close to the surface was intended for use in the lowest heat flux environments. Placement C, with the deepest thermocouples, was intended for use in the highest heat flux environments. Most models used placement B, which had intermediate thermocouple depths. Thermocouple placement option

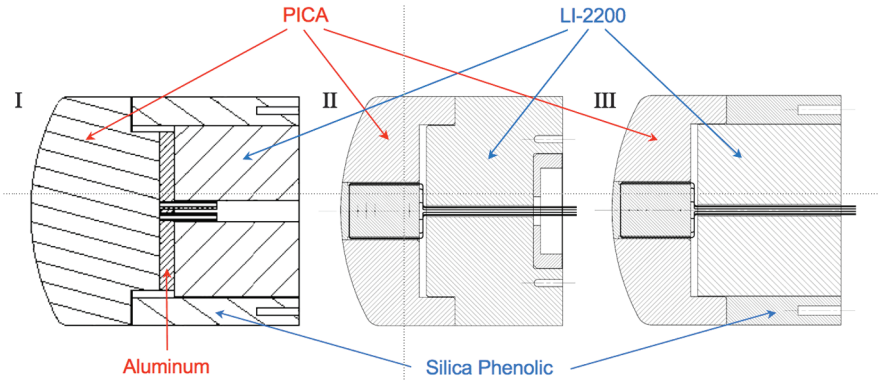

Fig. 4 Cross section of iso-q arcjet models. Model types II and III may contain a thermocouple plug (as shown). The initial thickness at the centerline varied from 3.49 to 4.13 cm.

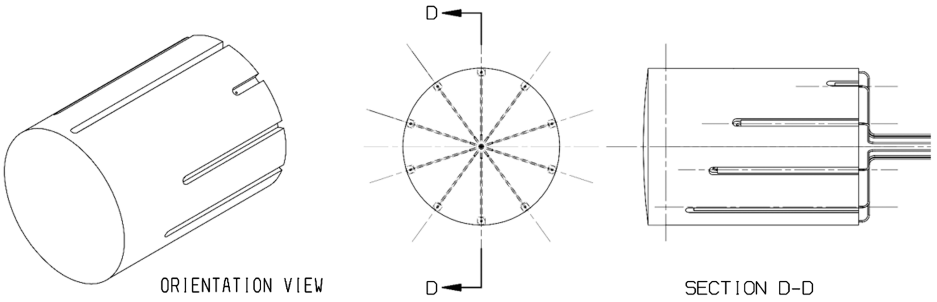

Fig. 5 Axial plug containing thermocouples 1 to 5 for model types II and III.

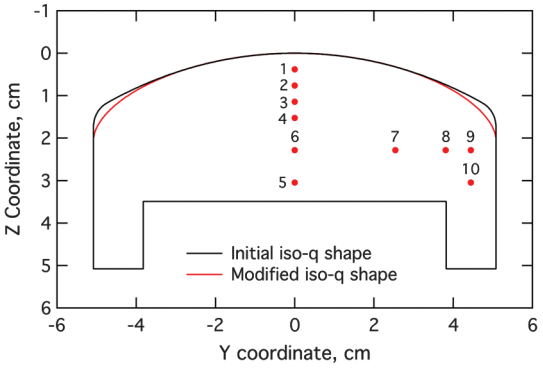

Fig. 6 Cross-sectional drawing of iso-q-shaped arcjet model with thermocouple locations for TC-placement options B and D (see Table 1). Thermocouples are not coplanar.

D includes the offaxis thermocouples that were used in two tests that will be thoroughly discussed in Sec. VI, Model Validation. X-ray images of all pretest models confirmed that thermocouples were installed within ±0.02 cm of the nominal locations.

Arcjet tests were conducted in the Aerodynamic Heating Facility (AHF) [17] and Interaction Heating Facility (IHF) [18] at NASA ARC and in the TP2 facility at NASA Johnson Space Center (JSC). For all test conditions multiple runs and multiple swing arms were used to obtain calibration measurements of stagnation pressure and cold-wall heat flux, and if possible, temperature response from multiple arcjet models with the same or different exposure durations. At the end of the exposure, the model was removed from the arcjet flowfield and held in a low-pressure environment during a cooldown period of several hundred seconds. For safety reasons, models are not exposed to atmospheric pressure until after they have cooled down.

The stagnation pressure and heat flux were measured using a combination slug-calorimeter/pitot-pressure device (Fig. 1) that had the same external shape as the TPS samples to be tested [19]. The calorimeter is inserted into the arcjet flow for approximately 3 s. Because the arcjet flow is both unsteady and swirling, there is natural variation in the stagnation measurements obtained from a short

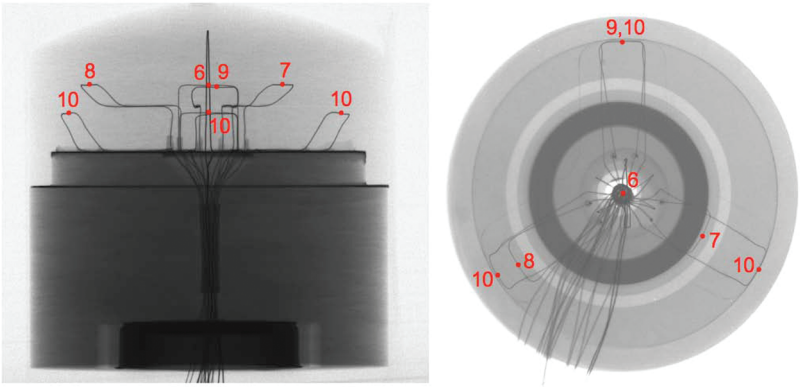

Fig. 7 Side-view and top-view x-ray images of arcjet model with thermocouple placement D.

Table 1 Nominal thermocouple locations within arcjet models. Depth is measured relative to the geometric stagnation point.

TC number	TC type	Radial location, cm	Axial depth for four TC placement options, cm			
			A	B	C	D
1	R	0.000	0.381	0.508	0.635	——
2	R	0.000	0.762	0.889	1.016	——
3	K	0.000	1.143	1.270	1.397	——
4	K	0.000	1.524	1.651	1.778	——
5	K	0.000	3.048	3.048	3.048	3.048
6	K	0.000	——	——	——	2.286
7	K	2.540	——	——	——	2.286
8	K	3.810	——	——	——	2.286
9	K	4.445	——	——	——	2.286
10	K	4.445	——	——	——	3.048

exposure even within the same arcjet run. Greater variation is seen on a run-to-run basis. The average stagnation measurements may not be representative of the average values experienced by any specific TPS sample that is tested for a longer time. The pressure measurements have less variability than the heat flux measurements. Based on previous experience with NASA arcjet facilities, we consider the uncertainty of the stagnation pressure to be less than $\pm 5\%$, and the uncertainty of the stagnation-point heat flux to be between ± 10 and $\pm 15\%$ [6]. The heat flux and pressure were not measured at any locations other than the stagnation point. We rely on CFD simulations to provide the variation of aeroheating conditions along the surface of test models.

In the ARC facilities argon is used to protect the upstream electrode, the main air is added along the length of the arcjet column, and additional air (called *add air*) may be injected after the downstream electrode. In the AHF facility there is a mixing chamber for add air between the downstream electrode and the nozzle. There is no such mixing chamber in the IHF. The total argon mass fraction in the flowfield depends on the three gas flowrates and the extent of add-air mixing into the core of the flowfield.

PICA models were exposed to 18 different test conditions, listed in Table 2. In the table, screening tests that used uninstrumented models are indicated by a footnote. Condition 18 is a dual-pulse test in which the model was exposed to one arcjet condition, removed from the flow for cool down in a partial vacuum, then reinserted for a second exposure at a different arcjet condition. The intent of this test was to approximate the nominal peak heat fluxes and heat loads for a lunar-return skip trajectory that has two heat pulses separated by a long cooldown period. In Table 2, the 13 rows without the footnote indicate tests that used models containing multiple thermocouples. The intent of these tests was to provide a broad range of heating conditions for development and validation of the material-response model. For nine conditions there were two exposure times that are designated as cases a and b, in order of increasing exposure time. Two columns are provided for the argon mass fraction at the centerline. For both columns we assume that the main air and argon are mixed. The minimum argon fraction is obtained if the add air also is assumed to mix perfectly into the flow. The maximum argon fraction is obtained if the add air is assumed not to mix into the core flow of main air plus argon. If the add-air flow rate is zero, then these two columns are the same. We note that dry air contains approximately 1.3% argon by mass.

The ARC stagnation conditions are plotted as gray dots in Fig. 8. The stagnation heat flux and pressure ranges are 107 to 1102 $\mathrm{W/cm^2}$ and 2.3 to 84.4 kPa, respectively. In general, the heat flux and pressure increase concurrently as the test conditions become more severe. Hence, the points cluster near the diagonal of the figure. However, add air may be used to increase the pressure and to reduce the heat flux. If the add-air flow is sufficiently high, then this process can produce points that lie significantly to the right of the diagonal corresponding to conditions 3, 5, and 7 in Table 2.

In the JSC facility, nitrogen is used to protect the upstream electrode, then both oxygen and nitrogen may be injected along the length of the arcjet to obtain a desired ratio of total oxygen to total nitrogen. The models were tested at four test conditions provided in Table 3. The stagnations conditions were approximately 412 $\mathrm{W/cm^2}$ at 18.3 kPa for all four conditions, but the ratio of total oxygen to total nitrogen was varied. The oxygen fraction at the centerline depends on the extent of gas mixing. The JSC conditions are shown as a cluster of four black dots in Fig. 8.

Both Table 2 and Table 3 contain two columns for enthalpy. The facility enthalpy is a value estimated from laminar flow heat transfer correlations based on the measured stagnation pressure and the cold-wall (calorimeter) heat flux [20]. The DPLR column provides the centerline enthalpy of the calculated flowfield. For the ARC facilities, these values differ in most cases by less than 10%. For the JSC facilities, the disagreement between the values is greater than 30%. This discrepancy is attributed to inaccuracy of the correlations for conditions in which the hot core of the arcjet flow is much smaller than the model diameter. The CFD-based enthalpy is considered to be the more reliable quantity and was used for all calculations presented in this work.

Table 4 provides a summary of all models tested, the thermocouple placement option (A to D or none), the measured centerline recession, and the maximum surface temperature. All PICA models were manufactured with the low conductivity direction parallel to the axis of symmetry. A total of 69 models were tested at 22 flow conditions. Forty-six of the models were instrumented with thermocouple plugs and tested at 17 conditions.

IV. Model Instrumentation and Measurements

In the arcjet tests at JSC, the models were too close to the nozzle exit plane to allow accurate visual observation with optical pyrometers. In most arcjet tests at ARC, the stagnation-point region was observed using two single-wavelength (one-color) pyrometers and one dual-wavelength (two-color) pyrometer. Raw pyrometer data were corrected for window and transmission losses, as applicable, and reported as a surface temperature. For the single-wavelength pyrometers, the data were corrected for temperature-dependent material emissivity. Because of the high emissivity of charred PICA, this correction is relatively small and varies from $+1.1\%$ at 2000 K to $+1.6\%$ at 3500 K. The intrinsic error of the one-color pyrometers after all corrections is estimated as $\pm 5\%$, based on previous experience with the ARC arcjet facilities. For the two-color pyrometer, there is no emissivity correction. The intrinsic error depends on the ratio of the spectral emittance at the two sensing wavelengths. For example, a 1% difference in emittance will result in an intrinsic error of about $\pm 7\%$ at 3500 K. For PICA the uncertainty is expected to be lower than this value.

In some tests, one or more pyrometers provided abnormal surface temperatures. There are several reasons why a pyrometer measurement may be too low. For example, the pyrometer may not be focused exactly on the stagnation point of the model; furthermore, as the material ablates, the hot surface may move in or out of focus during the course of the experiment. In contrast, it is unlikely for a pyrometer to provide a temperature that is too high, except for the intrinsic error of the device. In the tests reported herein, for multiple samples tested

Table 2 Arcjet test conditions at NASA ARC for mixtures of air and argon

Environment condition number	Facility and nozzle diameter, in.	Stagnation-point cold-wall heat flux, W/cm^2	Stagnation pressure, kPa	Facility estimated centerline enthalpy, MJ/kg	DPLR centerline enthalpy, MJ/kg	Main air, g/s	Add air, g/s	Argon, g/s	Minimum argon fraction (perfectly mixed)	Maximum argon fraction (unmixed add air)	Exposure time, s	Number of models
1	AHF 18	107	2.3	15.9	15.2	80	0	29	0.276	0.276	55	2
2ab[a]	AHF 18	143	3.8	17.0	16.5	150	0	29	0.173	0.173	200, 400	1, 1
3ab	AHF 7	154	13.3	9.7	8.4	80	50	28	0.188	0.269	33, 66	2, 1
4ab	AHF 18	169	5.0	17.8	17.0	200	0	30	0.142	0.142	33, 60	2, 3
5ab	AHF 7	190	45.7	7.2	7.3	140	470	46	0.082	0.257	30, 60	2, 1
6ab	AHF 18	246	8.5	20.0	19.3	340	0	36	0.108	0.108	42, 60	7, 2
7ab	AHF 7	255	29.8	11.1	11.1	160	140	34	0.113	0.186	30, 60	2, 1
8	IHF 13	395	17.2	22.8	21.4	450	0	33	0.080	0.080	34	2
9[a]	IHF 13	430	17.9	24.1	22.4	280	220	46	0.096	0.152	120	7
10ab	AHF 7	480	31.9	20.7	19.0	250	50	34	0.113	0.131	34, 68	2, 1
11ab	IHF 13	548	19.4	29.6	27.2	450	0	33	0.080	0.080	30, 40	3, 2
12	IHF 13	552	27.3	25.3	23.3	670	0	46	0.076	0.076	30	2
13[a]	IHF 13	712	33.2	29.4	26.7	720	50	68	0.093	0.098	70	8
14	IHF 13	744	31.0	32.0	29.2	719	50	52	0.076	0.080	27	1
15	IHF 6	762	46.6	26.6	23.7	175	200	29	0.084	0.153	45	2
16ab[a]	IHF 8	970	63.4	25.2	23.6	461	481	74	0.085	0.150	30, 40	2, 2
17	IHF 6	1102	84.4	28.7	25.6	270	330	42	0.078	0.146	10	1
18a[a]	IHF 13	425	16.2	23.8	22.2	300	200	41	0.088	0.132	113	2
18b[a]	IHF 13	161	9.2	12.6	12.5	130	200	29	0.093	0.193	128	2

[a]Screening tests that used uninstrumented models.

Fig. 8 Measured stagnation pressure and cold-wall heat flux for test conditions in Tables 2 and 3. Circled dots indicate seven cases to be discussed in detail.

at the same conditions, and excluding abnormal data, the corrected pyrometer temperatures were, in general, consistent within the assumed accuracy of ±5%. However, based on the preceding discussion, if multiple data sets are available, then the maximum pyrometer temperature may be the most reliable value.

In-depth temperatures were measured using multiple bare-wire type R and type K thermocouples installed as shown in Figs. 5–7. The thermocouple wire diameter was 0.25 mm. The thermocouple junctions were installed with at least 12.5 mm of wire aligned in a direction approximately parallel to the expected isotherm shape for axisymmetric heating. This installation method, with a length-to-diameter ratio of 25:1 on each side of the thermocouple junction, minimizes the error associated with temperature gradients in the wire [16]. Thermal lag effects due to the mass of the thermocouple are unavoidable but were minimized by using the thinnest practical wire diameter. With proper installation, temperature measurement errors for these in-depth thermocouple installations are estimated to be ±5%. The thermocouple depths and the arcjet exposure durations of most tests at ARC were selected to obtain a distribution of maximum temperatures at each test condition, with thermocouples located both in the char layer and in the pyrolysis zone. An additional goal was not to ablate more than one thermocouple, so that at least four thermocouples would provide data during the entire cooldown period.

Forty-six models, each containing five or more thermocouples, were tested. Very few thermocouples exhibited noisy or erratic response. The type R and type K thermocouples typically failed near their upper use temperatures of 2033 and 1643 K, respectively. In some models, the thermocouples continued to operate but provided poor data after a short exposure time near these temperature limits.

The use of unsheathed thermocouple wire can be problematic in dense carbonaceous materials due to their significant electrical conductivity. However, both virgin and charred PICA have sufficiently low electrical conductivity to mitigate this potential issue for the thermocouple spacing employed in this work.

The total recession of the arcjet models was determined by two methods. In the first method, the pre- and posttest samples were placed on a support frame, and the vertical height (Z) was measured at multiple locations in two perpendicular directions (X and Y) that pass through the axis of the model. The second method also employed a support frame; however, a fine-resolution laser scan of the vertical height was performed in the X and Y directions. For both methods, the pretest model was marked so that the posttest sample could be aligned with the same X-Y orientation that was used for the pretest measurements. The total recession was then calculated as the *difference* between the pre- and posttest Z values. In either method there may be a slight X-Y rotation or Z-axis offset between the pre- and posttest measurements. Therefore, it is difficult to determine small values of recession with precision, especially using the first method. In the central portion of the model, the recession values

Table 3 Arcjet test conditions at NASA JSC for mixtures of nitrogen and oxygen

Environment condition number	Facility and nozzle diameter, in.	Stagnation-point cold-wall heat flux, W/cm^2	Stagnation pressure, kPa	Facility estimated centerline enthalpy, MJ/kg	DPLR centerline enthalpy, MJ/kg	Nitrogen flow, g/s	Oxygen flow, g/s	Oxygen fraction (perfectly mixed)	Exposure time, s	Number of models
19	TP2 5	416	17.9	26.6	18.4	272	0	0	120	1
20	TP2 5	408	18.5	25.5	17.8	233	26	0.10	120	1
21	TP2 5	407	18.5	25.2	17.8	199	59	0.23	120	1
22	TP2 5	415	18.4	26.3	18.3	175	75	0.30	120	2

determined by the two methods agree, in general, to within an uncertainty of ± 0.5 mm.

Four examples of laser scans of models tested over a range of heat fluxes are shown in Fig. 9. For each of the four samples, the *X* and *Y* scans of pretest and posttest models are shown in the upper plot, and the difference between these curves is the recession shown in the lower plot. The lower figures also contain a black dot for the measured centerline recession with error bars. For some models the initial shape is asymmetric (although presumably within machining tolerance), and if the total recession is small, then this asymmetry is still visible in the posttest shape. This initial asymmetry is eliminated by the differencing operation used to calculate the recession. Nevertheless, the final recession distribution of a sample typically is asymmetric, and the amount of this asymmetry tends to increase with the severity of the test conditions and also with the use of add air, especially in the IHF.

A constricted arcjet flowfield is swirling and unsteady, both spatially and temporally. Although we desire that the unsteadiness and asymmetry average out over the duration of the exposure, and the flowfield is in fact simulated as axisymmetric and steady, this is clearly not the case. Slightly asymmetric shapes result from asymmetric average heating distributions that are a natural result of an arcjet experiment.

Some posttest samples were cross-sectioned, cleaned of cutting debris, and photographed from the direction perpendicular to the cut face. The photographs directly show the final ablated shape, and the color contours provide a qualitative measurement of the char depth. The color of partially charred PICA is not quantitatively related to density, because although the char is totally black, the virgin material varies in color. The material begins to develop a blackish hue when it is approximately 50% charred [21]. The shape of color variations in a photograph of the cross section should correlate with density contours that indicate the depth of thermal penetration minus the amount of material ablated.

V. Analysis Methodology

In this work, the DPLR code is used for simulation of the flow in the arcjet nozzle and around the test articles. The flow is assumed to be axisymmetric, laminar, steady, and nonswirling. The Navier–Stokes equations were solved on a multiblock grid for a six-species (N_2, O_2, NO, N, O, and Ar) gas mixture in thermal and chemical nonequilibrium. Reference [15] provides more information on the use of DPLR to simulate arcjet flows with stagnation-point models.

The integration between DPLR and FIAT or TITAN is based on a loosely-coupled approach. All DPLR solutions are computed for a cold, unblown, and fully-catalytic surface. For each surface node of the solution, local values of the pressure, the recovery enthalpy, and the cold-wall heat transfer coefficient are calculated, and then these parameters are passed as boundary conditions to FIAT and/or TITAN. The cold-wall heat transfer coefficient is the cold-wall heat flux divided by the difference between the recovery enthalpy and the wall enthalpy. Surface thermochemical interactions and blowing effects are incorporated in these material-response codes by use of ablation tables, a surface energy balance with heat transfer coefficient, and a blowing reduction parameter. The blowing reduction parameter may be input as a function of time and location based on DPLR results; however, for the laminar flows considered in this work, a constant value of 1/2 was used.

Both FIAT and TITAN contain a simple cooldown option for the surface energy balance. This cooldown boundary-condition option, which is used after the model is removed from the arcjet flow, allows the material to continue pyrolyzing and to radiate from its surface to the environment, but the surface ablation rate is set to zero. The assumption of zero ablation rate during cool down is justified, because the surface temperature quickly becomes too low for sublimation to be significant, and the pressure is too low to sustain heterogeneous surface reactions of carbon. Most calculations were run to a total time of 700 s from the initial exposure to the arcjet.

One-dimensional FIAT calculations only require boundary conditions at the stagnation point as a function of time. For iso-q models

Table 4 Test conditions, thermocouple placement option, centerline recession, and maximum temperature for each arcjet model

Environment condition number	Analysis case number	Exposure time, s	Model ID	TC option	Centerline recession, mm	Maximum surface temperature, K
1	1	55	AA-43-209-N	A	2.33	2033
1	1	55	AA-43-210-N	A	2.27	2041
2a	——	200	AT-008	None	12.66	2177
2b	——	400	AT-007	None	24.72	2196
3a	——	33	AA-44-210-N	B	2.93	2161
3a	——	33	AA-44-211-N	B	2.92	2174
3b	——	66	AA-44-212-N	B	5.61	2163
4a	——	33	AA-43-211-N	A	2.27	2243
4a	——	33	AA-43-212-N	A	2.20	2245
4b	2	60	AA-43-208-N	A	4.28	2248
4b	2	60	1403	D	4.58	2259
4b	2	60	1404	D	4.76	2284
5a	——	30	AA-44-204-N	B	4.78	1989
5a	——	30	AA-44-205-N	B	3.79	2004
5b	——	60	AA-44-206-N	B	8.81	2065
6a	3	42	AA-43-213-N	A	3.71	2407
6a	3	42	AA-43-215-N	A	3.65	2414
6a	3	42	AA-43-207-N	A	3.95	2401
6a	3	42	AA-43-216-N	B	3.52	2432
6a	3	42	AA-43-227-N	B	3.68	2419
6a	3	42	1405	D	4.12	2437
6a	3	42	1406	D	3.69	2417
6b	——	60	AA-43-223-N	A	5.21	2434
6b	——	60	AA-43-228-N	A	5.23	2409
7a	——	30	AA-44-201-N	B	3.87	2331
7a	——	30	AA-44-202-N	B	4.33	2320
7b	——	60	AA-44-203-N	B	8.52	2359
8	4	34	AA-43-219-N	B	4.61	2730
8	4	34	AA-43-218-N	B	4.43	2735
9	——	120	AT-011	None	16.45	2703
9	——	120	AT-019	None	18.66	2718
9	——	120	AT-025	None	19.06	2713
9	——	120	AT-026	None	19.03	2697
9	——	120	AA-40-001	None	17.71	2682
9	——	120	AA-40-002	None	17.64	2677
9	——	120	AA-40-003-N	None	16.25	2662
10a	——	34	AA-44-207-N	B	6.32	2757
10a	——	34	AA-44-208-N	B	6.58	2764
10b	——	68	AA-44-209-N	B	13.63	2738
11a	——	30	AA-43-221-N	B	4.18	2990
11a	——	30	AA-43-224-N	B	4.55	2923
11a	——	30	AA-43-226-N	B	4.30	2943
11b	——	40	AA-43-222-N	B	5.89	2988
11b	——	40	AA-43-225-N	B	5.92	2934
12	5	30	AA-43-233-N	B	5.41	2963
12	5	30	AA-43-234-N	B	4.97	2963
13	——	70	AT-012	None	12.57	2984
13	——	70	AT-020	None	14.56	3030
13	——	70	AT-027	None	15.00	3053
13	——	70	AT-028	None	15.33	3015
13	——	70	AA-40-003	None	13.82	2994
13	——	70	AA-40-004	None	11.58	2994
13	——	70	AA-40-001-N	None	13.79	2969
13	——	70	AA-40-002-N	None	12.83	2984
14	6	27	AA-44-218-N	C	5.13	3030
15	——	45	AA-44-223-N	C	12.74	3098
15	——	45	AA-44-224-N	C	12.91	3098
16a	——	30	AT-001	None	11.97	3020
16a	——	30	AT-004	None	11.33	3051
16b	——	40	AT-003	None	15.15	3020
16b	——	40	AT-005	None	15.56	3030
17	7	10	AA-44-219-N	C	4.84	3233
18a	——	113	AT-009	None	Not measured	2728
18b	——	128	AT-009	None	26.95	2218
18a	——	113	AT-010	None	Not measured	2738
18b	——	128	AT-010	None	27.05	2213
19	——	120	AA-44-214-N	B	1.75	Not measured
20	——	120	AA-44-216-N	B	12.0	Not measured
21	——	120	AA-44-213-N	B	20.5	Not measured
22	——	120	AA-44-215-N	B	24.1	Not measured
22	——	120	AA-44-229-N	B	23.9	Not measured

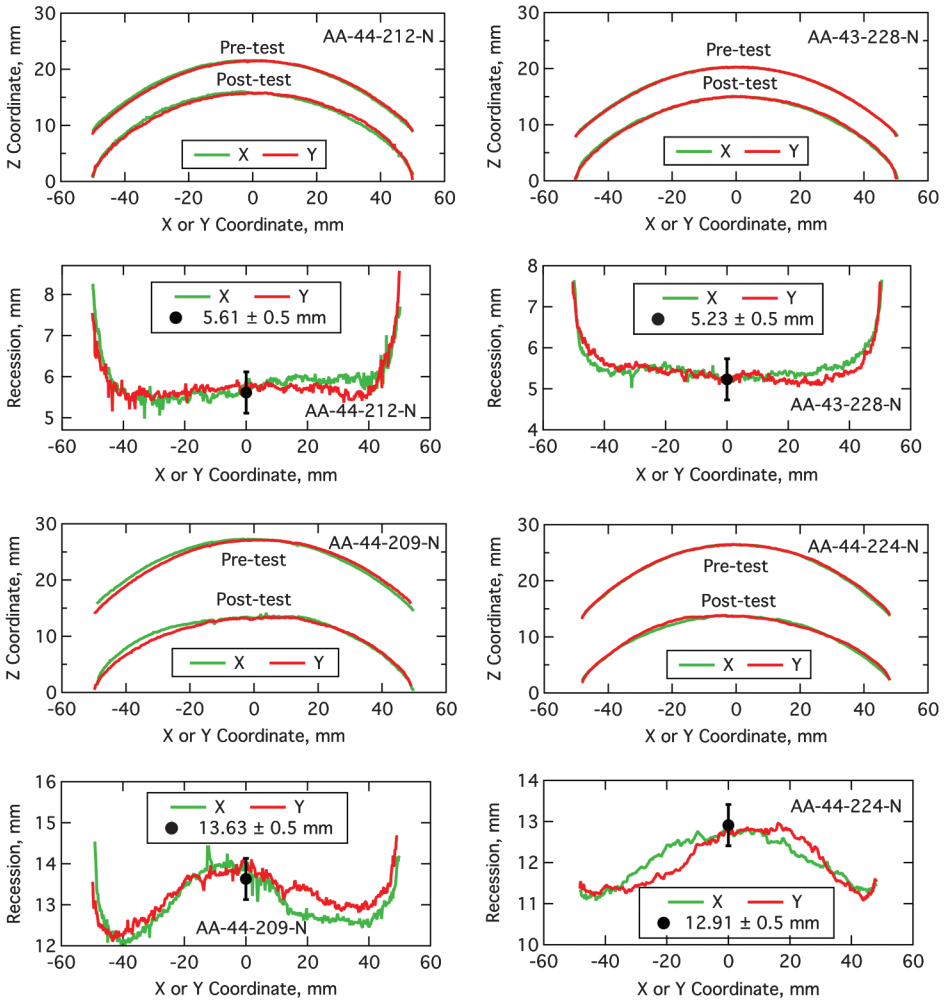

Fig. 9 Four examples of recession calculated from laser scan profiles. The black dot is the manually-measured centerline value.

tested at ARC, the relative shape change is small (cf. Fig. 3), and the initial boundary conditions may be used for the entire duration of arcjet exposure. For some tests at JSC, the shape change was significant, and DPLR solutions were also calculated for the final ablated shape. Boundary conditions were generated for the final exposure time, and the FIAT calculations interpolated the boundary-condition values for the initial and final times and shapes.

For both facilities, these one-dimensional calculations are accurate for stagnation-point temperature and recession and for temperatures at axial near-surface thermocouples during the arcjet exposure period. The calculations are not accurate for in-depth temperatures or for long time (especially during cool down) due to the effect of multidimensional heat conduction in PICA. A multidimensional analysis tool such as TITAN is required to obtain accurate predictions at greater times or depths, and furthermore, the transversely isotropic thermal conductivity of PICA must be taken into account [10].

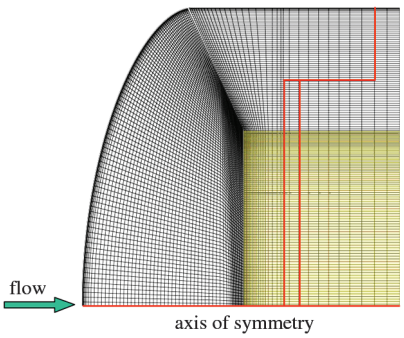

Fig. 10 Front portion of two-block TITAN grid for arcjet model of type II or III with modified iso-q shape. The interior block is shaded yellow.

For the two-dimensional TITAN calculations, the small peak in heat flux predicted by DPLR on the shoulder for the unablated shape (Fig. 2) causes the shoulder to change shape, which then alters the flowfield and heating distribution. The calculation cannot continue indefinitely with the original peaked heating profile, because within a few seconds the ablated surface would show an unrealistic indentation on the shoulder. To address this problem, TITAN calculations may be performed using two different approaches.

One approach [22] for conducting the simulation is to start with the original shape and heating distribution, and then, as needed, to calculate a series of new DPLR solutions using grids for increasingly ablated shapes during the course of the TITAN run. The initial flow field and its associated surface heat flux and pressure are first computed by DPLR. For each surface point, the local recovery enthalpy and the heat transfer coefficient are calculated, and then these parameters and pressure are passed as boundary conditions to TITAN. A time-accurate ablation and thermal-response computation is performed by TITAN. When the maximum surface recession meets a prespecified limit, TITAN stops its computation and outputs the location of the ablated surface. A new CFD grid is then generated for this ablated shape, and a new steady-state flow solution is calculated by DPLR. The pressure, recovery enthalpy, and heat transfer coefficient distributions are calculated for this new solution. The updated boundary conditions are input to TITAN for another run of time-accurate ablation and in-depth thermal response. This procedure is repeated until TITAN reaches the specified final time.

An alternative approach [10] is to slightly modify the initial shape near the shoulder to eliminate the local maxima in heat flux. The modified shape is shown as a red curve in Fig. 6. The modified shape

Table 5 Seven cases selected for detailed analysis

Analysis case number	Environment condition number	Stagnation-point heat flux, W/cm^2	Stagnation pressure, kPa	Exposure time, s
1	1	107	2.3	55
2	4b	169	5.0	60
3	6a	246	8.5	42
4	8	395	17.2	34
5	12	552	27.3	30
6	14	744	31.0	27
7	17	1102	84.4	10

has a more uniform heating distribution on the front face and no local maximum on the shoulder; however, the pressure drops off more rapidly with radius. The modified heating and pressure distributions, combined with the modified shoulder shape, allow a stable uncoupled calculation for the entire TITAN run at a fraction of the computational time required for the first approach. Reference [22] shows that this approximate method is quite accurate in computing in-depth temperature histories for iso-q-shaped models at ARC. All TITAN results presented in this work used this second approach.

TITAN calculation for models of type II and III use a two-block grid depicted in Fig. 10. The grid extends several centimeters to the right of the region illustrated in the figure. The exterior block, shown in black, is highly refined near the outer surface that is subject to aeroheating conditions. If surface recession occurs, the grid is compressed along the rays of the grid that intersect the heated surface. If pyrolysis occurs, the internal gas flow is assumed to be one-dimensional and quasi-steady along these rays. In the interior block, which is shaded yellow, the material may pyrolyze; however, there is no unique connection between the yellow rectangular cells and any specific ray of the external grid. Consequently, a TITAN calculation can retain its time accuracy only as long as ablation and the pyrolysis remain within the outer grid. This limitation prevents full application of TITAN to arcjet cases with large heat load or long exposure times such as conditions 2ab, 10b, 13, 15, 16, and 18–22 in Tables 2 and 3.

To present representative results across the range of conditions, seven primary cases corresponding to environment conditions 1, 4b, 6a, 8, 12, 14, and 17 were selected for detailed analysis and presentation in this work. These seven conditions are listed in Table 5 and marked as numbered circles around gray dots in Fig. 8. For each successive condition, the nominal heat flux increases by a factor of 35 to 60%.

In-depth thermal response along the centerline was calculated by FIAT results for all cases. The recession predictions from FIAT and TITAN at the axis agree to at least two digits, because for PICA the ablation near the centerline is insensitive to details of the in-depth conduction. The in-depth temperature response computed by FIAT becomes inaccurate with increasing time or depth; however, the results have some accuracy near the surface during the arcjet exposure period. FIAT in-depth temperature predictions will be presented for environment 21, in which a TITAN calculation was not feasible.

VI. Model Validation

The PICAv3.3 material model is used by the analysis codes FIAT and TITAN to predict the surface temperature and recession as well as the in-depth conduction and decomposition of the material in response to aeroheating. Extensive arcjet testing provided a huge amount of data that may be compared with model predictions. In this section, we consider sequentially the surface recession, the surface temperature, the in-depth temperatures, and the posttest char profile. For each item we discuss the seven primary analysis cases from Table 5 plus any notable results for other environments. All ablation calculations assume complete mixing of add air unless noted otherwise.

A. Ablation Model

Except for the most severe test conditions considered in this work, the ablation rate of PICA is dominated by the oxidation of carbon, which is highly sensitive to the oxygen concentration in the flow. Therefore, the equilibrium ablation tables were generated for ten different argon-air mixtures applicable to the various ARC test conditions and for four different oxygen-to-nitrogen ratios applicable to the JSC test conditions. Predicted total recession from FIAT for varying argon and six ARC test conditions is presented in Figs. 11a and 11b. As the argon fraction is increased, the oxygen fraction is decreased, and as expected the total recession also decreases. The magnitude of this decrease is greatest at higher heat fluxes (Fig. 11a), but the fractional decrease is greatest at the lowest heat flux (Fig. 11b).

We begin with comparisons of data and predictions for the seven cases in Table 5 that span the range of heat flux in the ARC arcjet tests. For each case, FIAT calculations were performed using the nominal aerothermal environment and also with a ±10% scaling factor applied to the heating. This factor is considered to be the *minimum* uncertainty of the arcjet environment. The predicted recession histories for the three heating levels for each case are presented in Figs. 12a–12g, in order of increasing heat flux. In all recession plots, the green, red, and blue curves are the FIAT predictions for 90, 100, and 110% of nominal heating, respectively, and the black circles are measured data points from Table 4 with uncertainty bars of ±0.5 mm. The range of recession that results

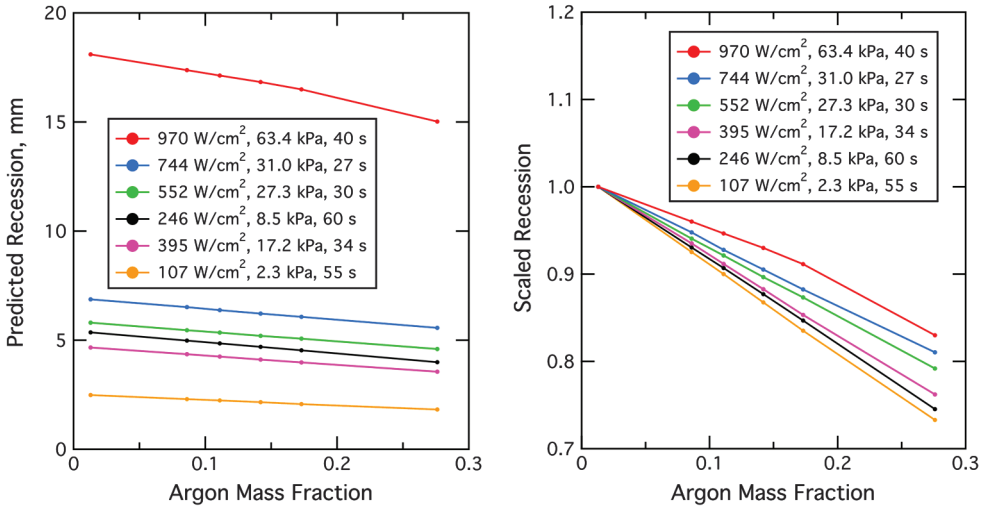

a) b)

Fig. 11 Effect of argon fraction for nominal (100%) heating on a) recession and b) scaled recession.

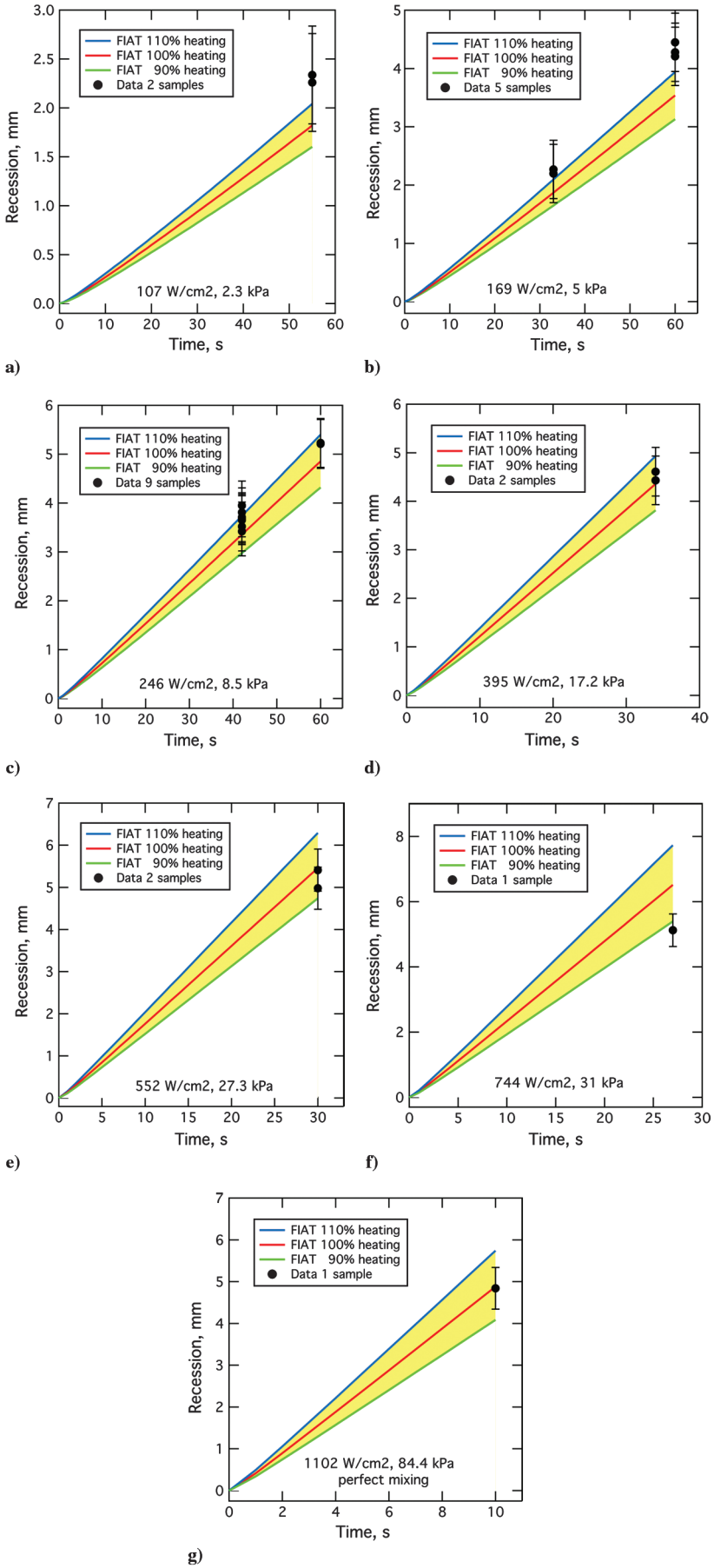

Fig. 12 Measured and predicted centerline recession with environmental uncertainty for a) case 1, b) case 2, c) case 3, d) case 4, e) case 5, f) case 6, and g) case 7.

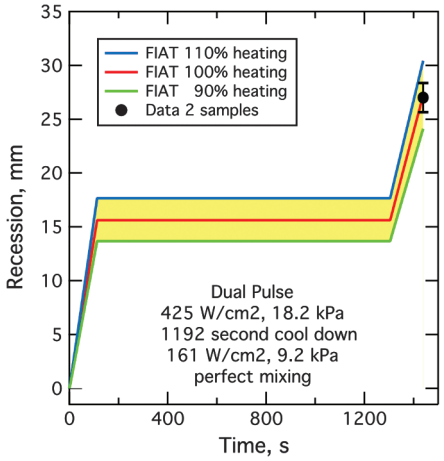

Fig. 13 Measured and predicted centerline recession for condition 18 with environmental uncertainty.

from the environmental uncertainty is shaded yellow. If the data points fall within the yellow-shaded region, then the ablation model cannot logically be assigned an error.

Case 1 at 107 W/cm^2 in Fig. 12a has the largest disagreement, with FIAT underpredicting the data points. The measured recession was about 2.3 mm, whereas FIAT predicts 1.5 to 2.1 mm. The FIAT curves are concave upward for the entire 55 s exposure, because the PICA material does not reach a condition of steady-state ablation very quickly at low heat fluxes. For case 2 at 169 W/cm^2 (Fig. 12b) FIAT underpredicts the data points, perhaps by a lesser extent than in case 1, and the curves have less upward curvature. For cases 3 to 5, at 246 to 552 W/cm^2, most data points fall within the range of the predictions. The curves become quite linear for heat flux above 300 W/cm^2, because at high heat fluxes PICA quickly reaches a steady state of ablation. Case 6 at 744 W/cm^2 (Fig. 12f) is an exception, in that the data point falls *below* the range of FIAT predictions. Only one sample was tested, and it is possible that this sample experienced a lower heat flux than the calorimeter. Case 7 at 1102 W/cm^2 (Fig. 12g) is the most severe environment, and the single data point lies in the center of the range of recession predicted by FIAT. For this environment, the material is primarily subliming rather than oxidizing.

For the notable dual-pulse test, condition 18, the models were exposed to two different heating environments in the same arcjet run. Figure 13 shows a very good agreement between the predictions and the data. The recession was not measured after the first heat pulse, because both test models remained inside the test chamber under partial vacuum between the two exposures to the arcjet flow. If similar tests are conducted in the future, we recommend for one sample to be exposed only to the first heating environment.

Results for condition 5 are ambiguous. If the add air is assumed to mix *perfectly* with the main-air flow, then the argon fraction at the centerline is 8%, and FIAT overpredicts the recession for two of three samples (Fig. 14a). Alternatively, if the add air is assumed *not* to mix with the main-air flow, then the argon fraction is 26% at the centerline, and FIAT underpredicts the recession for one sample at 30 s exposure (Fig. 14b). These recession predictions are consistent with the effect of argon discussed previously (cf. Fig. 11). Similar ambiguous results were calculated for AHF high-add-air conditions 3 and 7. This effect was found to be not as significant for IHF conditions 9, 15, and 16. Unfortunately, because there is no direct measurement of the gas composition near the axis of the flow, it is not possible to eliminate this additional environmental uncertainty at this time.

Compared with the ARC facilities, the enthalpy profile in the JSC arcjet is more peaked near the axis. Consequently, the iso-q models tend to flatten in the center as they ablate. Also the stagnation conditions vary more significantly along the centerline as the model recedes away from the arcjet nozzle exit plane. Both effects tend to decrease the stagnation heat flux as a function of time. For these reasons, it was necessary to perform additional DPLR flowfield calculations. For test conditions 19 to 22, DPLR solutions were obtained for both the unablated and an ablated shape (approximated by an ellipsoid) at two different axial locations that spanned the maximum total recession obtained in the JSC tests. The DPLR environments were interpolated by FIAT to take into account the decrease in heat flux due to recession and to shape change.

The FIAT results are compared with data for conditions 19 to 22, in Figs. 15a–15d, respectively. Each condition used different ablation tables that were generated for the appropriate oxygen fraction that varied from 0 to 30%. For three cases, the data are within the range predicted by FIAT, and for 10% oxygen, the data point is at the upper limit of the predicted range. For all four conditions the recession curves are concave downward, which is the opposite of the usual trend, because these calculations take into account the decrease in heat flux with time as discussed above.

The preceding discussion compared predictions of total recession with data from the arcjet models, where we assumed a minimal environmental uncertainty of $\pm 10\%$. If the recession measurement is inside the range of predictions, then the recession prediction error is defined as zero. If the measurement is outside the range of predictions, then the error may be defined as

$$E = \frac{(\Delta S_{\text{measured}} - \Delta S_{\text{FIAT}})}{(\Delta S_{\text{measured}})} \tag{1}$$

where the closest FIAT result is used in the formula. This error is positive if the calculation underpredicts the data and negative if FIAT

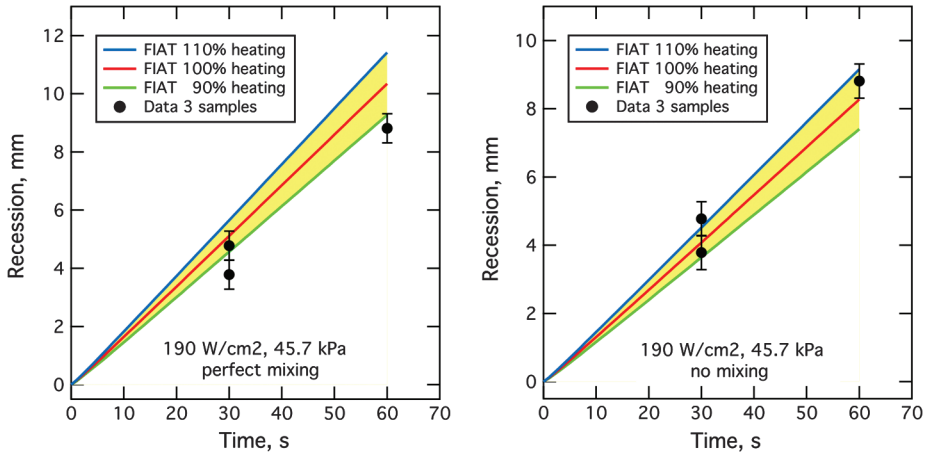

Fig. 14 Measured and predicted centerline recession with environmental uncertainty for condition 5 with a) perfect add-air mixing (8% argon) and b) no add-air mixing (26% argon).

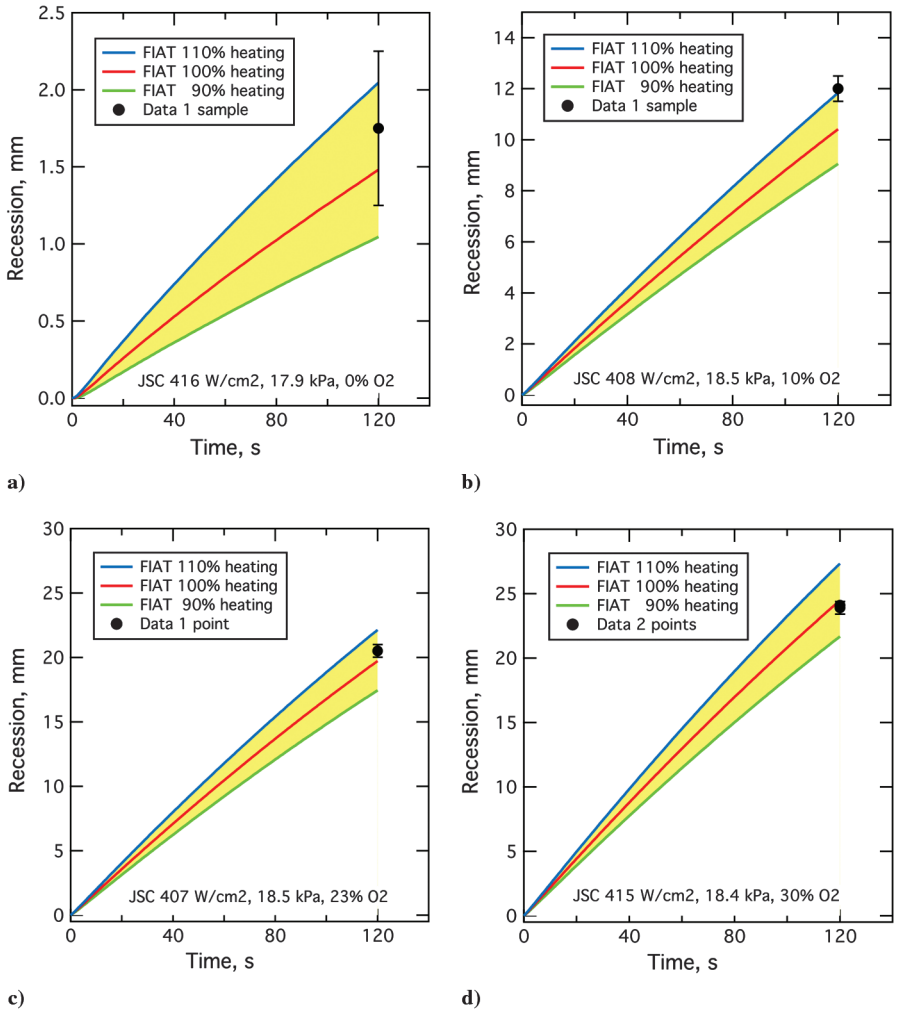

Fig. 15 Measured and predicted centerline recession with environmental uncertainty for a) condition 19, b) condition 20, c) condition 21, and d) condition 22.

overpredicts the recession. The recession prediction error was calculated for all samples using FIAT results for *perfect* mixing of the add air. The results are plotted as a function of stagnation heat flux and pressure in Figs. 16a and 16b, respectively. On both plots there are 47 points with zero error and 22 points with nonzero error.

As a function of heat flux (Fig. 16a), there is no obvious trend, except for apparent scatter of errors mostly below 200 W/cm^2. The error is bounded by the horizontal lines at ±12.5%, except for one point from condition 5a with low measured recession. This exceptional point is the high-add-air environment that was discussed

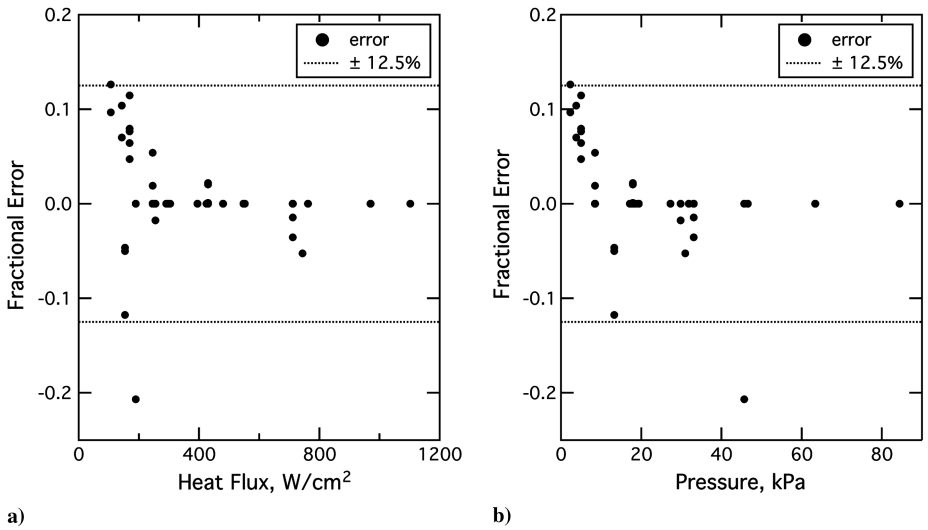

Fig. 16 Fractional error in recession prediction for all models in Table 4 as a function of a) heat flux and b) pressure. The error is positive if FIAT underpredicts the recession.

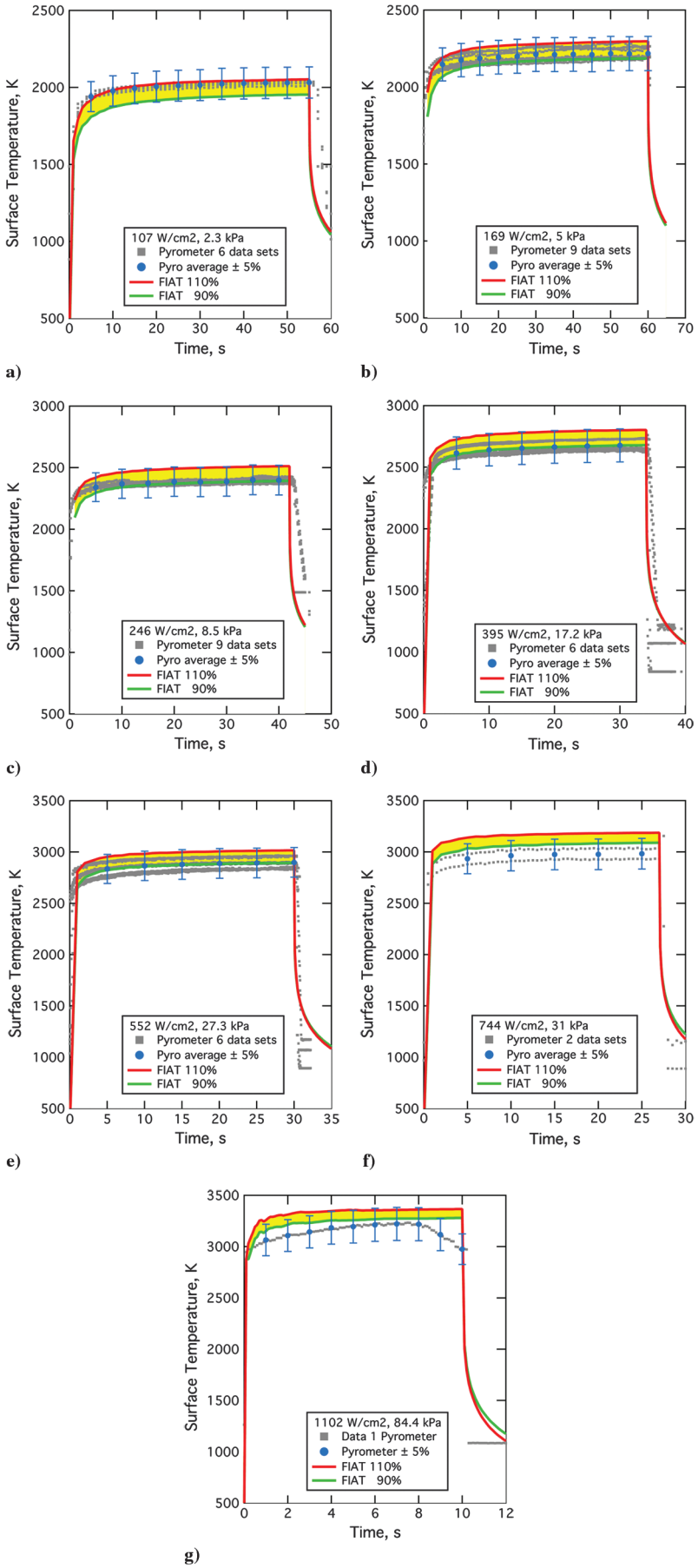

Fig. 17 Measured and predicted surface temperatures with environmental uncertainty for a) case 1, b) case 2, c) case 3, d) case 4, e) case 5, f) case 6, and g) case 7.

previously (Figs. 14a and 14b). If the add air is not perfectly mixed, the error for this data point may be any value between 0 and −21%.

As a function of pressure (Fig. 16b), the underpredicted points are clustered below 10 kPa. The largest errors are at conditions 1, 2, and 4 with pressure ≤ 5 kPa. The recession is expected to fall below the predictions of an equilibrium ablation model at sufficiently low surface temperatures, usually corresponding to heat fluxes below 90 W/cm^2, due to kinetic limitations to carbon oxidation. However, it is unusual for recession to exceed the predictions of an equilibrium model. For these very low-pressure cases, the DPLR flowfield shows that the boundary layer is frozen, yet the oxygen is almost fully dissociated. This phenomenon occurs because, in an arcjet flow, the oxygen is dissociated upstream of the shock, unlike in a flight environment, in which dissociation begins as the flow passes through the shock. In the arcjet at sufficiently low pressure, the oxygen recombination rate is too low for oxygen atoms to equilibrate within the boundary layer. We believe the measured recession exceeds the predictions of the equilibrium model due to the excessively high concentration of atomic oxygen reaching the surface. Development of a kinetic ablation model for PICA that is applicable to these low-pressure arcjet environments is an area of ongoing research [13].

B. Surface Temperature

As mentioned in the preceding subsection, for all test environments, FIAT calculations were performed using the nominal aerothermal environment and also with a ±10% scaling factor applied to the heating. The predicted surface temperature histories are shown in Figs. 17a–17g, in order of increasing heat flux for the seven cases in Table 5. In all surface temperature plots, the green and red curves are the FIAT predictions for 90 and 110% of nominal heating, respectively, and the region between these curves is shaded yellow. The gray squares are surface temperatures derived from pyrometer temperatures. The blue symbols are the average of the pyrometer data with ±5% error bars. In many tests, useful data were obtained from three different pyrometers. The pyrometers observe the stagnation-point region only while the model is located on the axis of the flowfield. Therefore, any data obtained before or after the model is centered in the flow are not a measurement of the stagnation-point temperature.

For the first five cases between 107 and 552 W/cm^2, in Figs. 17a–17e, the average pyrometer reading falls within the range predicted by FIAT. The amount of scatter of the pyrometer data varies on a run-to-run basis, but is less than the assumed uncertainty of ±5%. For case 6 at 744 W/cm^2 (Fig. 17f), only one sample was tested and one of the one-color pyrometers failed to provide usable data. The FIAT predictions lie above the data obtained from the other two pyrometers. The FIAT prediction at 90% heating is within 5% uncertainty of the average pyrometer reading. This result is consistent with the recession results reported previously (Fig. 12f) that suggested that this particular sample (ID no. AA-44-218-N) experienced a lower heat flux than measured by the calorimeter. For case 7 at 1102 W/cm^2 (Fig. 17g), only one sample was tested, and only one pyrometer was aimed toward the stagnation model. The other pyrometers were pointed at different locations in order to observe a large wedge model that was tested in the same arcjet run. This one pyrometer may not have been properly focused at the stagnation point, because the data does not smoothly reach a plateau as seen in the all other cases. Nevertheless, the FIAT predictions lie within the uncertainty range of the maximum pyrometer temperature.

The maximum surface temperature from the pyrometer data for every sample is listed in the last column of Table 4. Two maxima were obtained for each sample tested in the dual-pulse test (environments 18a and 18b). The results are compared in Fig. 18 with the maximum FIAT temperatures calculated for each environment. The plot is not a continuous function, primarily because the exposure durations vary from run to run. The pyrometer data inexplicably appear to plateau near 3000 K for heat fluxes between 500 and 1000 W/cm^2, whereas the predictions show an increasing trend in this range of heat flux.

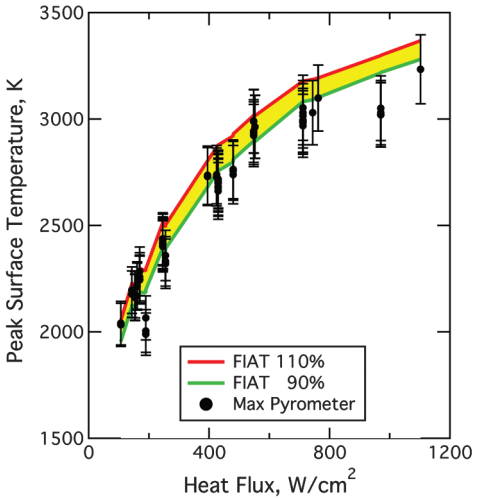

Fig. 18 Measured and predicted peak surface temperature for all conditions.

Except for two environments, the FIAT predictions are within the uncertainty of the data. These exceptions are environments 5 and 16, in which all pyrometers are significantly below the predictions. For the latter environment, the test models had a smaller diameter, and it is possible that the pyrometer data are not as accurate in this particular case. The former environment is the high-add-air case mentioned previously. Unlike recession predictions (Figs. 14a and 14b), the surface temperature prediction is relatively insensitive to the degree of add-air mixing, and it is therefore unclear why add air should have any effect on pyrometer measurements. However, it is possible that high add air may adversely affect the quality of the flowfield (e.g., the enthalpy profile) in a manner that is not currently modeled in our simulations.

C. Thermal Response

Initial calculations of the in-depth thermal response were performed using the FIAT code. For all test conditions, comparisons with data showed good agreement with thermocouple data only for relatively small times and depths. This discrepancy was attributed to multidimensional conduction effects. This hypothesis was confirmed by performing axisymmetric analysis with the TITAN code, using aerothermal boundary conditions distributions obtained from the DPLR flowfield solutions. Calculations were performed using 90, 100, and 110% scaling of the nominal aerothermal environments. However, it is difficult to present results for multiple thermocouple locations and multiple environmental scalings on the same plot. Therefore, results will be presented only for the nominal environment, that is, 100% heating, unless otherwise noted.

Two samples were tested at condition 1. Figure 19a shows data and predictions for near-surface thermocouples TC1 to TC3 up to 160 s, and Fig. 19b presents the data and predictions for TC3 to TC5 on a longer time scale. In these figures, the thermocouple data from the two samples are red and blue lines, the TITAN predictions are black lines, and FIAT predictions are green lines. TITAN provides a good match to both the magnitude and the time scale of the thermal response at all five TC locations, including the cooldown period up to 500 s. Although the time scale looks correct in the FIAT calculation, the magnitude of the predicted response is too low, especially for deep TC5. Clearly, the one-dimensional calculation underpredicts the amount of thermal energy within the sample. The reason for this disagreement is fairly obvious; during arcjet exposure the model is heated along the whole exterior surface. The model sides have a larger surface area than the front face, and as shown previously, the heat flux is significant along the sides. Therefore, there is a substantial heat load on the sides that increases the in-depth temperatures above the level predicted by a one-dimensional analysis. Thermal penetration in the radial direction is enhanced by the relatively high in-plane thermal conductivity of PICA.

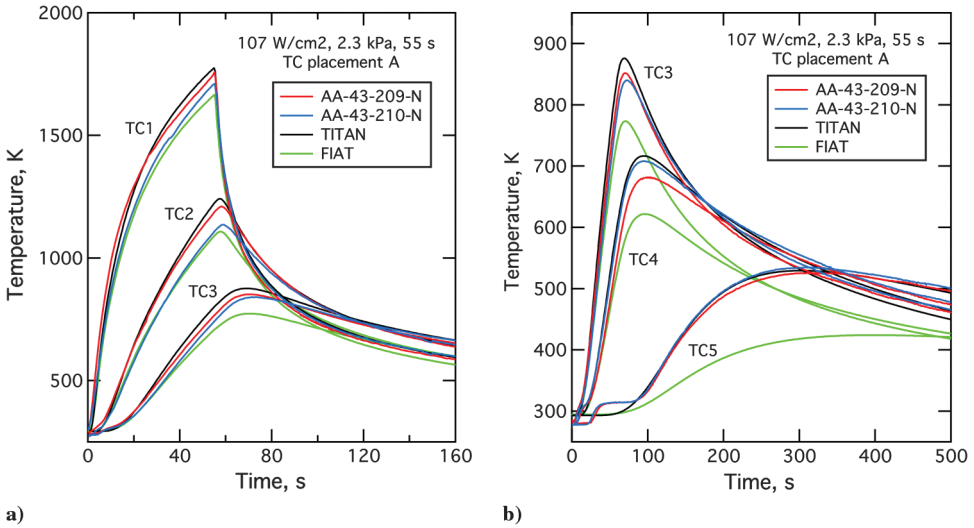

Fig. 19 Measured and predicted in-depth temperatures for case 1: a) thermocouples 1 to 3 and b) thermocouples 3 to 5.

The measured in-depth temperatures from this and from all other PICA tests are characterized by a small temperature increase to approximately 330 K followed by a plateau or decrease until the conduction heat pulse reaches the depth of the thermocouple. In most cases, a small blip may be discerned in the data from TC3 and TC4, whereas an obvious hump is present in the data from TC5. This phenomenon has been observed in previous PICA testing [6] and is believed to be a small exothermic reaction within the phenolic phase. This phenomenon apparently is not related to oxidation, because it is also seen when the material is tested in pure

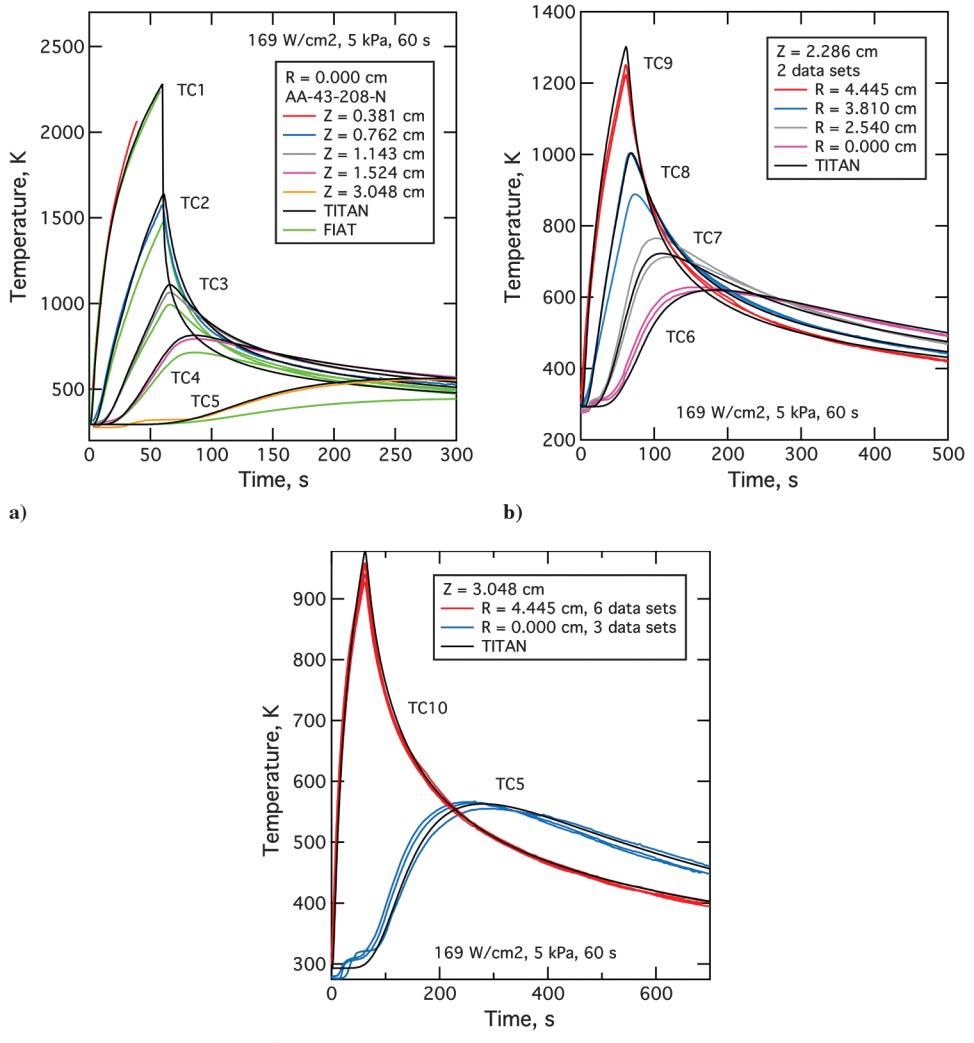

Fig. 20 Measured and predicted in-depth temperatures for case 2: a) axial thermocouples 1 to 5, b) thermocouples at an initial depth of 2.286 cm, and c) thermocouples at an initial depth of 3.048 cm.

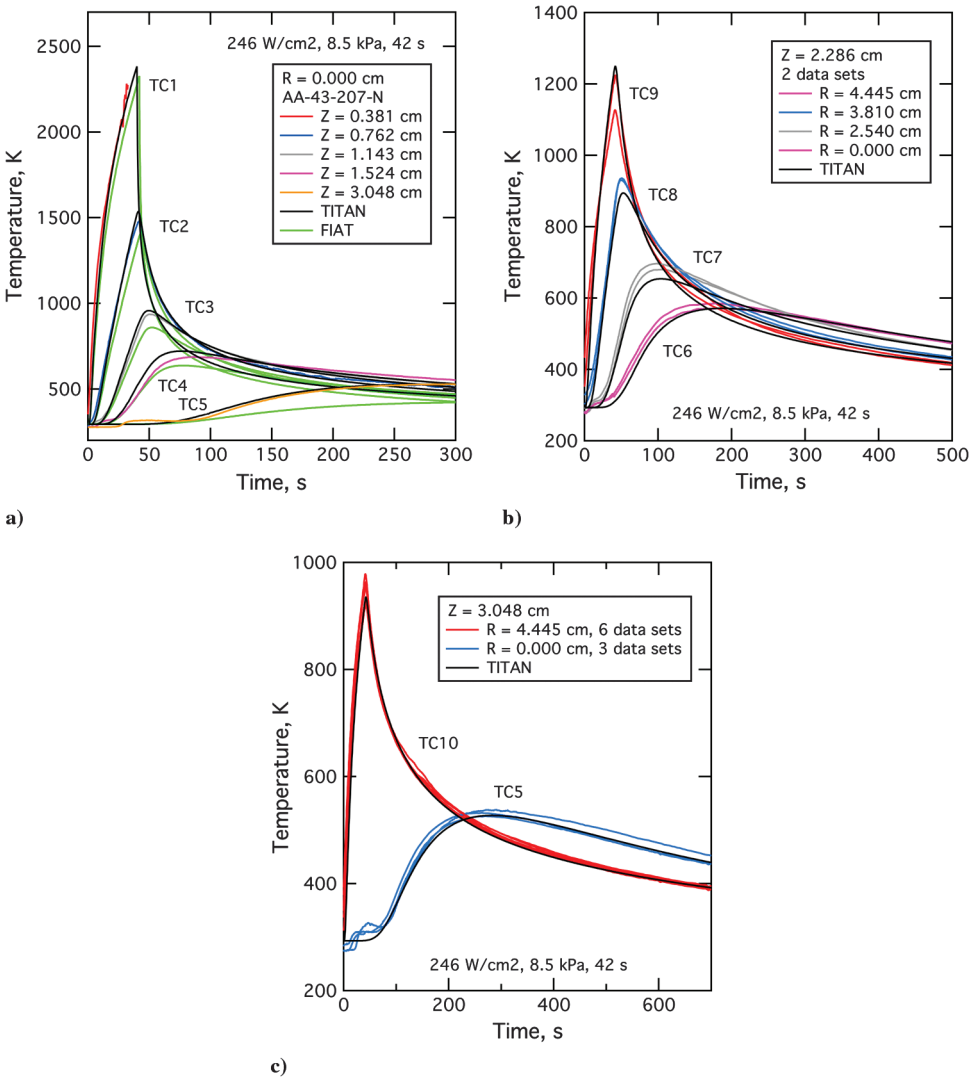

Fig. 21 Measured and predicted in-depth temperatures for case 3: a) axial thermocouples 1 to 5, b) thermocouples at an initial depth of 2.286 cm, and c) thermocouples at an initial depth of 3.048 cm.

nitrogen. Modeling of this reaction is outside the scope of the current work.

For condition 4b at 169 W/cm^2, PICA samples with both axial and radial thermocouples were tested. For this condition, the data are plotted with a different color for each thermocouple. TITAN predictions are black lines, and FIAT predictions are green lines. Axial thermocouples TC1 to TC5 are shown in Fig. 20a, and thermocouples at two different depths are given in Figs. 20b and 20c.

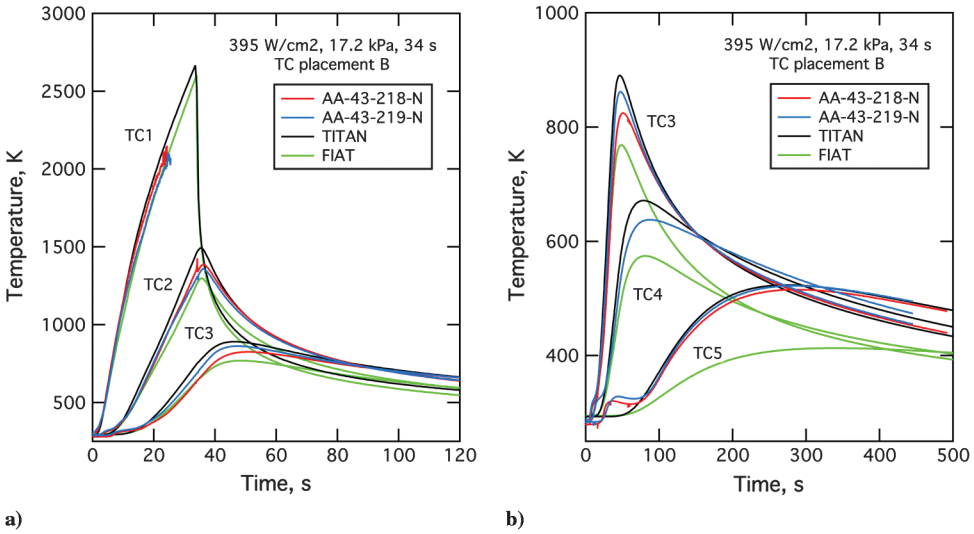

Fig. 22 Measured and predicted in-depth temperatures for case 4: a) thermocouples 1 to 3 and b) thermocouples 3 to 5.

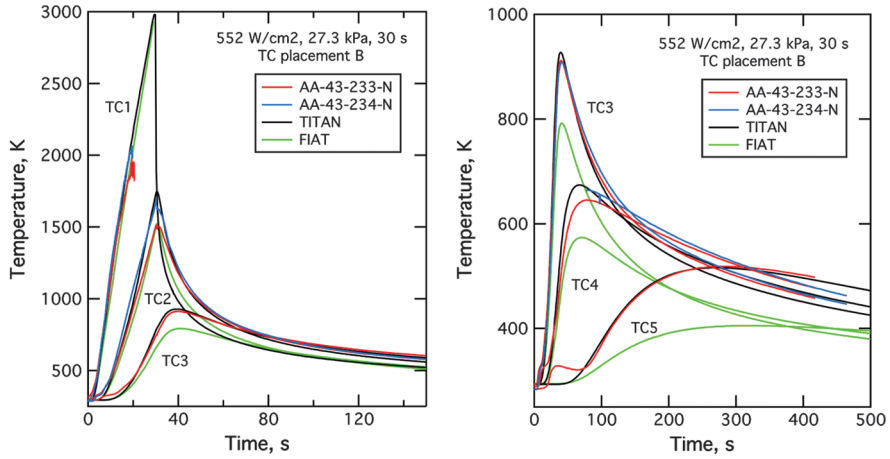

Fig. 23 Measured and predicted in-depth temperatures for case 5: a) thermocouples 1 to 3 and b) thermocouples 3 to 5.

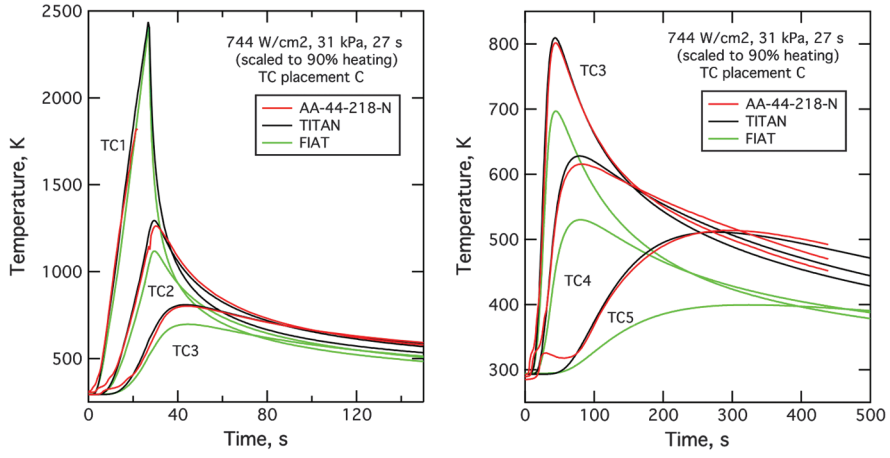

Fig. 24 Measured and predicted in-depth temperatures for case 6 with 90% scaling: a) thermocouples 1 to 3 and b) thermocouples 3 to 5.

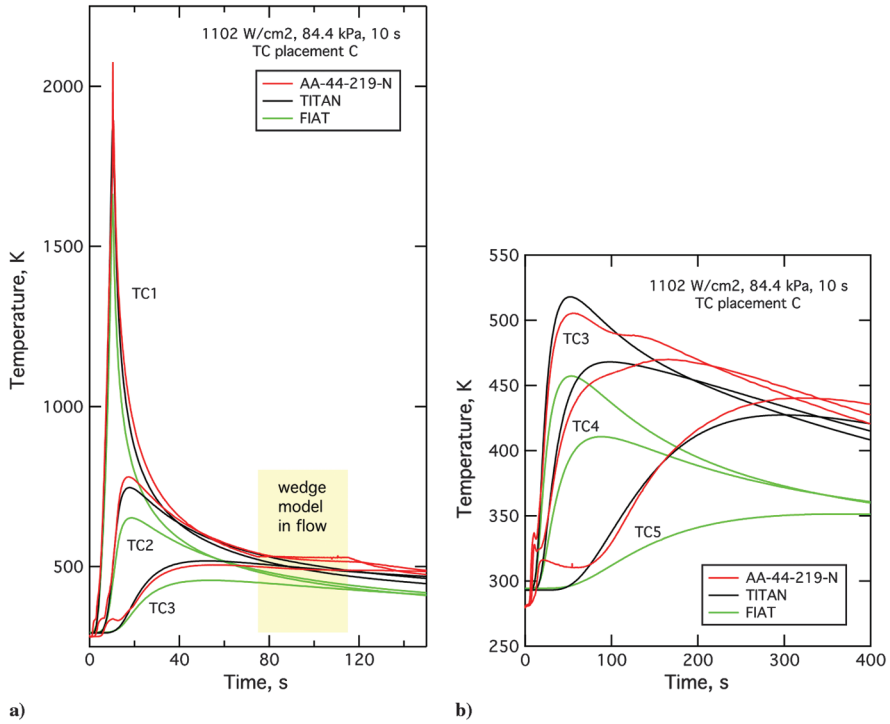

Fig. 25 Measured and predicted in-depth temperatures for case 7: a) thermocouples 1 to 3 and b) thermocouples 3 to 5.

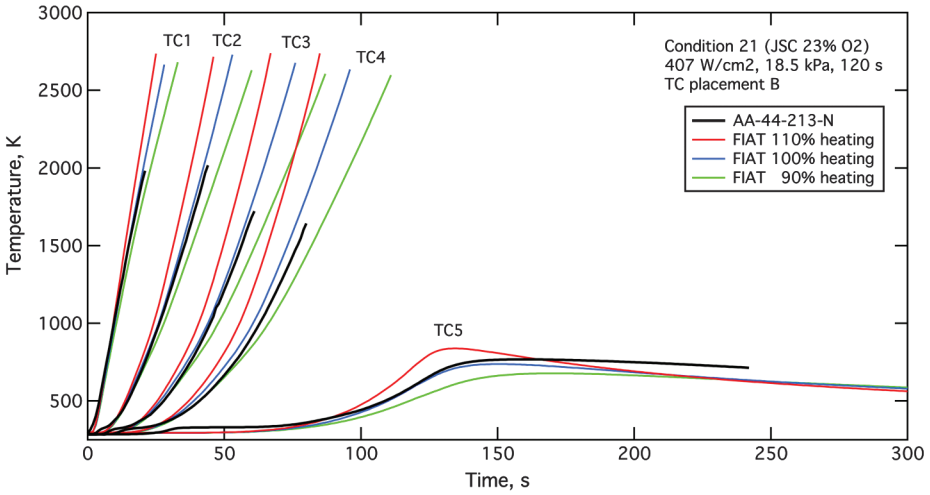

Fig. 26 Measured and predicted in-depth temperatures for thermocouples 1 to 5 at condition 21.

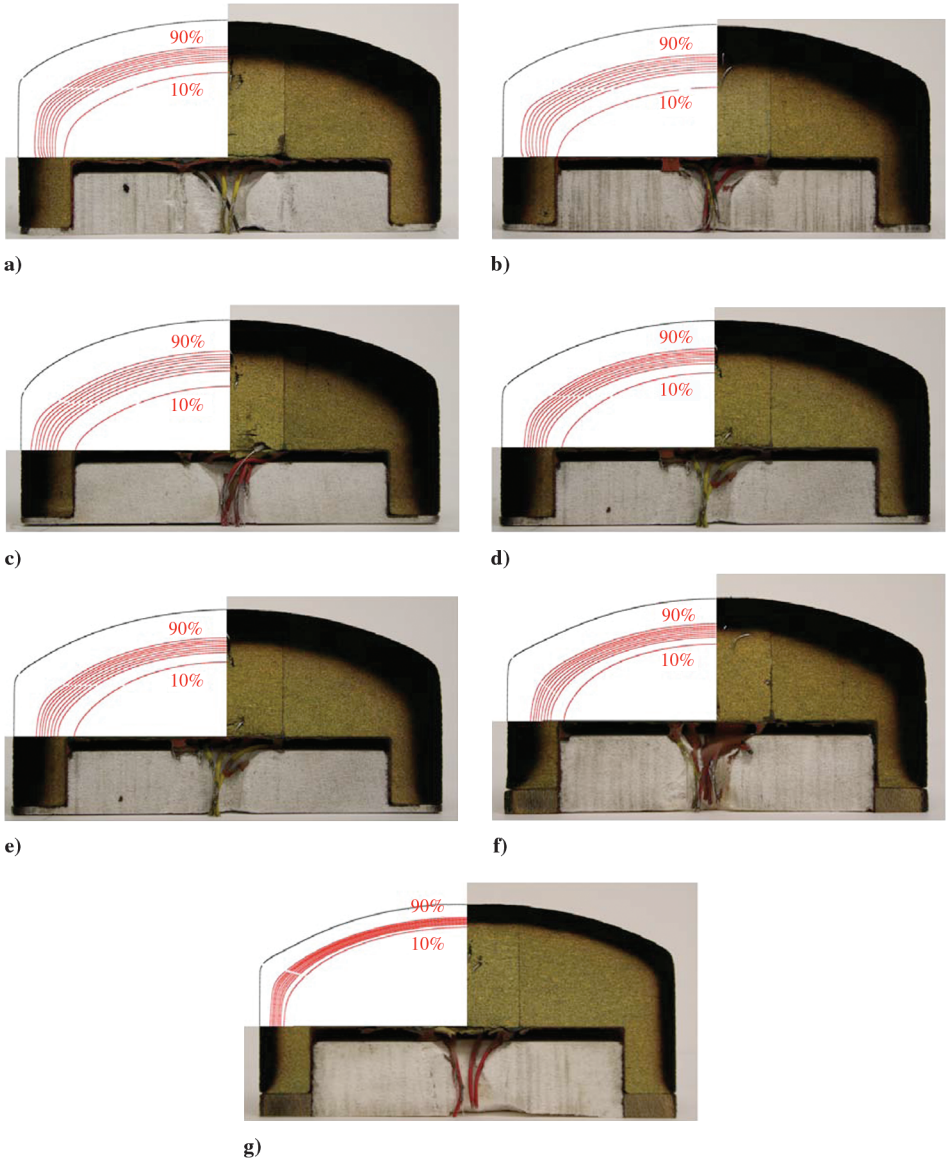

Fig. 27 Comparison of predicted shape and density contours with model cross section for a) case 1 at 107 W/cm^2 for 55 s, b) case 2 at 169 W/cm^2 for 60 s, c) case 3 at 246 W/cm^2 for 42 s, d) case 4 at 395 W/cm^2 for 34 s, e) case 5 at 552 W/cm^2 for 30 s, f) case 6 with 90% scaling of 744 W/cm^2 for 27 s, and g) case 7 at 1102 W/cm^2 for 10 s. Nine contours indicate 10 to 90% charred material.

The near-surface thermocouple TC1 failed near 2000 K. For all ten thermocouple locations, the TITAN simulation provides an excellent match to the data. The agreement is particularly impressive during the cooldown period out to 700 s in Fig. 20c. The small temperature hump at short time is visible in the data from TC4 and TC5.

A similarly excellent agreement between data and predictions was obtained for case 3 (condition 6a) at 246 W/cm^2. Axial thermocouples TC1 to TC4 are shown in Fig. 21a, and thermocouples at two different depths are given in Figs. 21b and 21c. Again, the agreement is impressive during the cooldown period out to 700 s in Fig. 21c.

For cases 4 to 7, the data are plotted in the same manner as in case 1. Results for case 4 at 395 W/cm^2 and case 5 at 552 W/cm^2 are presented in Figs. 22a and 22b and in Figs. 23a and 23b, respectively. TITAN provides a reasonable match to all TCs, whereas the FIAT predictions for the deeper TCs fall increasingly below the data as the heat flux is increased.

For case 6 at 744 W/cm^2 the TITAN results for 100% heating overpredicted the temperature response at TC1 and TC2. However, both the surface recession and the surface temperature results suggest that this model experienced a lower heat flux than the calorimeter measurement. Therefore, TITAN was rerun using 90% scaling of the aerothermal heat flux. The computed temperatures using 90% scaling agree well with the thermocouple measurements as shown in Figs. 24a and 24b.[¶]

Results for the highest heat flux case at 1102 W/cm^2 for 10 s are presented in Figs. 25a and 25b. TITAN provides a reasonable match for TCs 1 to 3 for 75 s. Between 75 and 115 s, a large wedge model was tested. This time interval is indicated by the yellow shading in Fig. 25a. The stagnation model, although not directly in the arcjet flowfield, clearly experienced additional heating during this time, as indicated by the unusual plateau in the TC1 data. This additional heating may be a result of both flow deflection and radiation from the wedge model. As a consequence of the additional heat load, the data from the deeper TCs rise above the TITAN predictions during the cooldown period after 100 s.

As a final example of the conduction model, Fig. 26 presents FIAT predictions and thermocouple data for condition 21. For this case, the TC data are presented as black curves, and FIAT predictions for 90, 100, and 110% of nominal heating are green, blue, and red curves, respectively. One sample was tested at JSC in simulated air with 23% oxygen. The exposure duration of 120 s was excessive for this model design; consequently, almost 60% of the model ablated, including the four thermocouples closest to the surface. The type R and type K thermocouples appear to fail near 2000 and 1650 K, respectively. Only the deepest thermocouple survived the arcjet exposure. The data fall within the range of the FIAT predictions up to 160 s, after which time FIAT underpredicts the data for TC5.

In the past, the in-depth thermal response of PICA in arcjet models was difficult to model accurately using one-dimensional analysis tools. The calculations presented herein clearly demonstrate that the one-dimensional analyses are inadequate because the thermal response is strongly affected by multidimensional conduction. The new PICAv3.3 thermal and ablation model, which takes into account transversely isotropic material properties, combined with multidimensional thermal analysis and CFD-based boundary conditions, provides a good agreement with in-depth temperature data across the entire range of stagnation test conditions considered in this work.

D. Ablated Shape and Char Depth

One posttest sample was cross-sectioned and photographed for each of the seven primary analysis cases. The ablated shape and in-depth density contours were plotted from the TITAN solutions at the final time (700 s). These photographs and plots are compared in Figs. 27a–27g for the seven cases, in order of increasing heat flux. The TITAN results are shown on the left side of each figure. Nine density contours representing 10 to 90% charred material are drawn on each TITAN plot. The 10% contour, which corresponds to near-virgin material, has the greatest in-depth penetration. The 90% contour, which corresponds to highly charred material, has the least in-depth penetration. The eight density contours, for 20 to 90% charred material, tend to cluster and thereby provide an indication of the location and thickness of the pyrolysis zone. For all seven cases, the clustered TITAN contours match the visual location of the pyrolysis zone, both on the axis and at the sidewall.

The posttest char depth shows the thermal penetration *minus* the amount of material ablated. The former increases with exposure duration, whereas the latter increases with heat flux. Except for cases 1 and 2, the exposure duration in these tests was decreased as the heat flux was increased. The net result of these conflicting trends is that the posttest char depth decreases with increasing heat flux. The char is thinnest in case 7 at 1102 W/cm^2, because the exposure duration was only 10 s.

VII. Conclusions

Data were presented from stagnation arcjet tests conducted on iso-q-shaped PICA models. These models were tested in the AHF and IHF facilities at NASA ARC and in the TP2 facility at NASA JSC at 22 test conditions spanning stagnation-point heat fluxes of approximately 100 to 1100 W/cm^2 and including different gas compositions. In-depth temperatures were measured at five to ten different locations including both axial and offaxis thermocouples. For most samples, the surface temperature was measured using three different pyrometers. Posttest recession was measured by two methods, and selected models were cross-sectioned to reveal the char depth.

A new ablation and thermal-response model, that includes transversely isotropic and pressure-dependent thermal conductivity, was developed based on extensive thermal, mechanical, and general property testing of newly manufactured PICA. One-dimensional FIAT and two-dimensional TITAN simulations of the ablation and thermal response of PICA were performed for the entire set of arcjet test conditions, using as boundary conditions the aerothermal environments predicted by the DPLR code. The simulations took into account the variations in gas composition and an estimated uncertainty of $\pm 10\%$ for heat flux.

The effect of gas composition, in particular dilution of oxygen by argon or nitrogen, is significant in prediction of recession of a carbonaceous ablator such as PICA. In this work, the argon mass fraction varied from 0 to 27%, depending on the facility and the test conditions. To obtain accurate recession predictions, it was necessary to generate many sets of ablation tables, with each set applicable only to a narrow range of gas compositions, so that for every analysis case, the appropriate set of tables could be selected.

With the exception of one sample, recession predictions using ablation tables for the applicable gas composition were within $\pm 12.5\%$ of measured values, after the nominal environmental uncertainty was taken into account. The use of add air changes the oxygen fraction by an unknown amount, depending on the degree of add-air mixing into the core of the flow. The uncertainty of gas composition was an additional complication for interpretation of results at three AHF test conditions, including the condition with the one sample mentioned above.

Comparisons of in-depth predictions with data show that one-dimensional modeling is inadequate, because the thermal response is strongly influenced by multidimensional heat conduction. Using the multidimensional and transversely isotropic thermal conductivity model with CFD-based boundary conditions, the in-depth thermal response was well predicted by TITAN.

Thermal penetration as indicated by char depth in cross sections also was qualitatively predicted. For 17 of the 19 exposure environments with pyrometer data, surface temperature predictions were within $\pm 5\%$ uncertainty of the average pyrometer measurement.

In future tests, if a quantitative recession measurement is desired, test durations sufficient to achieve at least 5 and preferably 8 to 10 mm of recession are recommended. Such test durations may be

[¶]Environment condition 14 (analysis case 6) was recently repeated for testing of a different TPS system. The average heat flux measurement was 694 W/cm^2.

excessive for validation of thermal-response models. In this case, multiple exposure durations should be used to provide useful data for both purposes.

The use of argon with air significantly complicates the modeling and analysis process. Different ablation tables are required, depending on the arcjet argon fraction, and these arcjet tables are different from the tables used for flight analyses. Furthermore, if add air is used, then the amount of argon at any location in the flowfield is indeterminate and depends on the degree of gas mixing. We recommend eliminating the use of argon. If nitrogen is used to shield the upstream electrode, then a calibrated amount of oxygen may be added in the upstream portion of the arcjet to achieve the correct ratio of nitrogen to oxygen for air. This recommended process would eliminate both the need for multiple sets of ablation tables and the ambiguity of element fractions caused by the use of add air.

Acknowledgments

The authors greatly appreciate the assistance of P. Agrawal, M. Olson, and especially K. Skokova for arcjet test data and that of T. Gokcen and D. Prabhu for DPLR analyses of arcjet flowfields. This work was supported by the Orion TPS Advanced Development Project.

References

[1] Tran, H., Johnson, C., Rasky, D., Hui, F., Chen, Y.-K., and Hsu, M., "Phenolic Impregnated Carbon Ablators (PICA) for Discovery Class Missions," AIAA Paper 96-1911, June 1996.

[2] Willcockson, W. H., "Stardust Sample Return Capsule Design Experience," *Journal of Spacecraft and Rockets*, Vol. 36, No. 3, 1999, pp. 470–474. doi:10.2514/2.3468

[3] Beck, R., Driver, D., Wright, M., Laub, B., Hwang, H., Slimko, E., Edquist, K., Sepka, S., Wilcockson, W., and Thames, T., "Development of the Mars Science Laboratory Heatshield Thermal Protection System," AIAA Paper 2009-4229, June 2009.

[4] Scott, A., Berry, S. A., Horvath, T. J., Lillard, R. P., Kirk, B. S., and Cassady, A. M., "Aerothermal Testing for Project Orion Crew Exploration Vehicle," AIAA Paper 2009-3842, June 2009.

[5] Tran, H. K., Johnson, C. E., Rasky, D. J., Hui, F. C. L., Hsu, M.-T., Chen, T., Chen, Y.-K., Paragas, D., and Kobayashi, L., "Phenolic Impregnated Carbon Ablators (PICA) as Thermal Protection Systems for Discovery Missions," Appendix C, NASA TM 110440, April 1997.

[6] Covington M. A, Heinemann, J. M., Goldstein, H. E., Chen, Y.-K., Terrazas-Salinas, I., Balboni, J. A., Olejniczak, J., and Martinez, E. R., Erratum, "Performance of a Low Density Ablative Heat Shield Material," *Journal of Spacecraft and Rockets*, Vol. 45, No. 4, 2008, pp. 854–864. doi:10.2514/1.38249

[7] Covington M. A, Heinemann, J. M., Goldstein, H. E., Chen, Y.-K., Terrazas-Salinas, I., Balboni, J. A., Olejniczak, J., and Martinez, E. R., "Erratum on Performance of a Low Density Ablative Heat Shield Material," *Journal of Spacecraft and Rockets*, Vol. 45, No. 6, 2008, p. 1330. doi:10.2514/1.40598

[8] Chen, Y.-K., and Milos, F. S., "Ablation and Thermal Analysis Program for Spacecraft Heatshield Analysis," *Journal of Spacecraft and Rockets*, Vol. 36, No. 3, 1999, pp. 475–483. doi:10.2514/2.3469

[9] Chen, Y.-K., and Milos, F. S., "Two-Dimensional Implicit Thermal Response and Ablation Program for Charring Materials," *Journal of Spacecraft and Rockets*, Vol. 38, No. 4, 2001, pp. 473–481. doi:10.2514/2.3724

[10] Milos, F. S., and Chen, Y.-K., "Two-Dimensional Ablation, Thermal Response, and Sizing Program for Pyrolyzing Ablators," *Journal of Spacecraft and Rockets*, Vol. 46, No. 6, 2009, pp. 1089–1099. doi:10.2514/1.36575

[11] Chen, Y.-K., Gökçen, T., and Edquist, K. T., "Two-Dimensional Ablation and Thermal Response Analyses for Mars Science Laboratory Heatshield," AIAA Paper 2009-4235, June 2009.

[12] Milos, F. S., and Chen, Y.-K., "Comprehensive Model for Multicomponent Ablation Thermochemistry," AIAA Paper 97-0141, Jan. 1997.

[13] Milos, F. S., Chen, Y.-K., and Gökçen, T., "Nonequilibrium Ablation of Phenolic Impregnated Carbon Ablator," AIAA Paper 2010-981, Jan. 2010.

[14] Wright, M. J., Candler, G. V., and Bose, D., "Data-Parallel Line Relaxation Method for the Navier–Stokes Equations," *AIAA Journal*, Vol. 36, No. 9, 1998, pp. 1603–1609. doi:10.2514/2.586

[15] Prabhu, D., Saunders, D., Oishi, T., Skokova, K., Santos, J., Fu, J., Terrazas-Salinas, I., Carballo, E., and Driver, D., "Analysis Framework for Arc-Heated Flowfields, I: Stagnation Testing in Arc-jets at NASA ARC," AIAA Paper 2009-4080, 2009.

[16] "Standard Practice for Internal Temperature Measurements in Low-Conductivity Materials," ASTM International, Std. E-377-08, West Conshohocken, PA, 2008.

[17] Balter-Peterson, A., Nichols, F., Mifsud, B., and Love, W., "Arc Jet Testing in NASA Ames Research Center Thermophysics Facilities," AIAA Paper 1992-5041, Dec. 1992.

[18] Winovich, W., and Carlson, W., "The 60-MW Shuttle Interaction Heating Facility," *Proceedings of the 25th International Instrumentation Symposium*, Instrument Society of America, Pittsburgh, PA, 1979, pp. 59–75.

[19] "Standard Test Method for Measuring Heat-Transfer Rate Using a Thermal Capacitance (Slug) Calorimeter," ASTM International, Std. E-457-08, West Conshohocken, PA, 2008.

[20] Zoby, E. V., "Empirical Stagnation-Point Heat-Transfer Relation in Several Gas Mixtures at High Enthalpy Levels," NASA TN D-4799, Oct. 1968.

[21] Stackpoole, M., Sepka, S., and Cozmuta, I., "Post-Flight Evaluation of Stardust Sample Return Capsule Forebody Heatshield Material," AIAA Paper 2008-1202, Jan. 2008.

[22] Chen, Y.-K., Milos, F. S., and Gökçen, T., "Loosely Coupled Simulation for Two-Dimensional Ablation and Shape Change," *Journal of Spacecraft and Rockets*, Vol. 47, No. 5, 2010, pp. 775–785. doi:10.2514/1.39667

K. Wurster
Associate Editor